Irreversible electrochemical reaction at high voltage induced by distortion of Mn and V structural environments in Na4MnV(PO4)3

Sunkyu Park, Jean-Noël Chotard, Dany Carlier, François Fauth, Antonella Iadecola, Christian Masquelier, Laurence Croguennec

Irreversible Electrochemical Reaction at High Voltage Induced by Distortion of Mn and V Structural Environments in $Na_4MnV(PO_4)_3$

Sunkyu Park [1,2,3], Jean-Noël Chotard [1,5], Dany Carlier [2,5], François Fauth [4], Antonella Iadecola [5], Christian Masquelier [*,1,5] and Laurence Croguennec [*,2,5]

[1] *Laboratoire de Réactivité et de Chimie des Solides, Université de Picardie Jules Verne, CNRS-UMR 7314, F-80039 Amiens Cedex 1, France*

[2] *CNRS, Univ. Bordeaux, Bordeaux INP, ICMCB UMR 5026, F-33600 Pessac, France*

[3] *TIAMAT, 15 Rue Baudelocque, F-80000 Amiens, France*

[4] *CELLS-ALBA Synchrotron, Cerdanyola del Vallès, E-08290 Barcelona, Spain*

[5] *RS2E, Réseau Français sur le Stockage Electrochimique de l'Energie, FR CNRS 3459, F-80039 Amiens Cedex 1, France*

Corresponding authors

Laurence Croguennec : Laurence.Croguennec@icmcb.cnrs.fr

Christian Masquelier : Christian.Masquelier@u-picardie.fr

Abstract

As the importance of developing low cost and high capacity materials is emerging, Mn-based $Na_4MnV(PO_4)_3$ positive electrode materials that allow multi redox reactions are in the spotlight for Na-Ion batteries. The structure that gives highly reversible electrochemical reactions, when two Na^+ (out of four) are de-inserted, deteriorates rapidly when the third Na^+ is extracted at high voltage, resulting in poor cyclability. In this work, using synchrotron-based *operando* techniques, we perform long range and local structural analyses to determine the origins of the rapid structural decay of $Na_4MnV(PO_4)_3$ when the third Na^+ is extracted. *Operando* XRD shows a significant change in the crystal structure (*c* parameter increases rapidly) as the occupancy of the Na(1) site decreases at high voltage. The local environments of Mn and V, monitored by *operando* XAS remain rather symmetrical up to two Na^+ extraction, while both Mn and V show drastic local distortions when the third Na^+ is extracted. These structural degradations are found to further progress when cycling to high voltage. This study presents important aspects of how local and long range structure modifications can affect the electrochemical performance in multi redox NASICON materials.

Introduction

The NASICON (Na-superionic-conductor)-type materials described by a 3D framework structure and the chemical formula of $A_xMM'(XO_4)_3$ (A = Li, Na; X = P, S, Si, Mo, W) are extensively studied for Na-ion batteries because of their thermal stability, rate performance, and cycle life.[1,2,2–7] $Na_3V_2(PO_4)_3$ for instance, when used as a positive electrode material, is characterized by a reversible electrochemical reaction involving the exchange of two Na^+ through the $V^{4+/3+}$ redox couple at 3.4 V (vs. Na^+/Na) via a two-phase reaction, for a theoretical capacity of 118 mAh/g.[8–12] To increase this moderate capacity, new NASICON-type materials capable of multi-redox reactions, *i.e.*, possibly allowing more than 1 Na^+ exchange per transition metal, such as $Na_{3+x}MM'(PO_4)_3$ (MM'= FeV,[13–16] MnV,[17–25] and MnCr [26–29]), have been extensively studied in recent years.

When Goodenough and his coworkers first reported on the $Na_4MnV(PO_4)_3$ compound, limited but highly reversible electrochemical reaction with two Na^+ extraction / insertion was demonstrated when the cutoff voltage was set to 3.7 V vs. Na.[17] After that, it was revealed by two studies at about the same time that additional Na^+ (*i.e.*, more than 2 Na^+) can be extracted depending on the upper-cutoff voltage.[18,19] These discoveries prompted interest in the $Na_4MnV(PO_4)_3$ positive electrode material due to the foreseen huge energy density increase, and many follow-up studies were conducted.[18–25] When $Na_4MnV(PO_4)_3$ is operated electrochemically in a wide potential window, about 3 Na^+ can be extracted through three distinct voltage domains during the charge of the battery with the expected activation of the $V^{4+/3+}$, $Mn^{3+/2+}$, and $V^{5+/4+}$ redox couples.[18–20,23] However, it was shown that the voltage profile of the following discharge changes to a complete sloping voltage curve due to an irreversible structural modification.[18–20,23] It was envisaged that amorphous phases formed at high voltage impacted on the capacity decay, hindering Na^+ diffusion and interfacial charge transfer.[23] However, the highly de-intercalated phase obtained at high voltage has not been investigated in detail yet, especially its local environments, remaining thus still unclear.[23] In addition, the mechanism of Na^+ re-insertion with the sloping voltage profile after the deep charge has not been well understood. When the $Mn^{2+}Cr^{3+}$ and $Fe^{2+}V^{3+}$ systems are

operated at high voltage, capacity retentions are better than that observed for the MnV system.[13–16,18–20,23,26–29] It has been anticipated that Mn^{3+} Jahn-Teller distortion is expected to affect capacity retention for $Na_xMnV(PO_4)_3$,[20,21,24,25,30,31] but no experimental evidence properly supported this assumption yet.

To improve the stability of the Mn/V-mixed NASICON materials, substitution by electrochemically inactive Mg^{2+} or Al^{3+} was tried, or by more than two elements such as Ti^{4+}, V^{3+}, Cr^{3+}, Mn^{2+}, Fe^{2+}, Zr^{4+}, but capacity fading could not be avoided.[16,22,31–33] It was suggested, through the study on $Na_3CrV(PO_4)_3$, that the irreversible structure modification at high voltage could be partially recovered when over-discharged to a low voltage.[34] The structural investigation of the MnV system when discharged to such a low voltage has not been explored yet. Therefore, in this study, we deeply investigate the Na^+ extraction/insertion mechanism in $Na_4MnV(PO_4)_3$, and the structural evolution at the long range and local scales depending on the voltage windows, by combining *operando* synchrotron X-ray powder diffraction and X-ray absorption spectroscopy. Also, the aging mechanism of the $Na_4MnV(PO_4)_3$ material is addressed when an extended voltage window is applied. This study provides important insights in designing Mn- or V-based multi-electron NASICON materials with increasing specific energy density while maintaining their excellent structural stability.

Experimental

***Synthesis*:** $Na_4MnV(PO_4)_3$ was prepared using a sol-gel assisted solid-state reaction method. Na_2CO_3 (Sigma-Aldrich, 99.5 %) and $NH_4H_2PO_4$ (Sigma-Aldrich, 98.5 %) were dissolved in a molar ratio of 2:3 in deionized water (solution A). Then a solution of $Mn(CH_3COO)_2{\bullet}4H_2O$ (Fluka, 99 %), $C_{10}H_{14}O_5V$ (Sigma-Aldrich, 97 %), and citric acid (Alfa Aesar, 99 %) was prepared in a molar ratio of 1:1:2 in deionized water and ethanol (50/50 by volume) using a magnetic stirrer (solution B). Then solution A was added dropwise into solution B with constant stirring and temperature at 80°C using an oil bath, followed by further drying in an oven. The resulting powder was heat-treated at 400 °C for 4 hours with the heating rate of 5 °C/min in Ar, then the powder

was recovered and ground in a mortar, followed by annealing at 800 °C for 10 hours with the heating rate of 2 °C/min in Ar.

Material Characterization: The chemical composition of the synthesized material was determined using inductively coupled plasma-optical emission spectroscopy (ICP-OES) with a Varian Model 720-ES spectrometer. The standard solutions of Na (Agilent, 1001±2 mg/L), Mn (SCP Science, 1004±4 mg/L), V (SCP Science, 1004±5 mg/L) and P (SCP Science, 1003±5 mg/L) were used for calibrations. The quantity of carbon coating on the synthesized material was determined by thermogravimetric analysis (TGA) with a NETZSCH STA 449C. Adiabatic calorimetry was used to monitor a phase transition of the synthesized material with PerkinElmer 8000 in aluminum crucibles with a scan range of 248 - 573 K at a heating and cooling rate of 10 K /min. The powder's morphology was examined by scanning electron microscopy (SEM) with a Hitachi Model S-4500 microscope.

Electrochemical Measurements**:** The working electrodes were prepared by mixing the $Na_4MnV(PO_4)_3$ powder and carbon black (Alfa Aesar, 99.9+%) with a weight ratio of 80:20 before being dried overnight at 80 °C under vacuum. The carbon black powder was pre-dried at 250 °C under vacuum before use. CR2032-type coin cells were used with a half-cell configuration in which Na metal was used as a counter electrode. The electrolyte was composed of 1 M $NaPF_6$ in ethylene carbonate (EC) / dimethyl carbonate (DMC) (1:1, w/w) with 2 wt.% of fluoroethylene carbonate (FEC) and one sheet of each Whatman glass fiber (GF/D) and Celgard was used as a separator. Battery assemblies were done in Ar-filled glove box (MBraun).

X-ray Powder Diffraction**:** Laboratory X-ray powder diffraction (XRPD) was performed using Cu $K\alpha_{1,2}$ radiation either in Debye-Scherrer geometry using a 0.3-mm capillary (PANalytical Empyrean) or in Bragg-Brentano geometry using airtight sample holder (PANalytical Empyrean). Synchrotron X-ray powder diffraction (SXRPD) measurements were performed on the MSPD beamline of the ALBA synchrotron in Spain.[35] The SXRPD patterns were recorded every ~30 minutes by averaging several scans with an acquisition time of ~3.5 minutes for each scan in the 2θ angular range of 2–40°, with a 2θ step size of 0.006° with a wavelength of 0.8266

Å using Debye−Scherrer geometry with a MYTHEN detector. The SXRPD patterns of several *ex situ* samples were collected with a 0.3-mm capillary, prior to the *operando* measurements. *Operando* SXRPD measurements were performed with an *in situ* coin cell with two glass windows.[36] The working electrode was made of the $Na_4MnV(PO_4)_3$ and conductive carbon additive with a ratio of 80/20 in wt.% with the mass loading of the active material of 6.6 mg/cm^2. The *in situ* cell was assembled using the same electrolyte and separator than those used in conventional coin cells as described just above, with a half-cell configuration versus Na metal. The *in situ* cell was cycled in a voltage window of 1.0 – 4.3 V vs. Na^+/Na with a C-rate of C/9 (1 Na^+ in 9 h). Diffraction data analysis was performed using the FullProf Suite.[37] The evolution of the unit cell volume per formula unit (*V*/*Z*) was analyzed with the profile matching method and several selected SXRPD patterns were analyzed with the Rietveld method. As Na^+ occupancy and the atomic displacement parameter are very highly corelated, refinements were carried out carefully: the crystallographic parameters of each atomic site were first refined one by one while fixing others. The occupancy ratios and isotropic displacement parameters were refined alternatively and finally all the parameters were refined at the same time.

X-ray absorption spectroscopy **(XAS)**: Synchrotron XAS measurements were performed at manganese and vanadium K-edges in transmission mode at the ROCK beamline of the SOLEIL synchrotron (France).[38] Reference samples available for Mn ($Mn^{2+}SO_4$ and $Mn^{3+}OOH$) and V ($Na_3V^{3+}_2(PO_4)_3$, $Na_1V^{4+}_2(PO_4)_3$) were measured to assign the oxidation states of Mn and V, respectively. *Operando* XAS spectra at Mn and V K-edges were recorded on the same electrode made of $Na_4MnV(PO_4)_3$, carbon black (Alfa Aesar, 99.9+%) and polytetrafluoroethylene (PTFE, Sigma-Aldrich, 99.9 %) as a binder, with a weight ratio of 73/18/9 and the mass loading of 8.5 mg/cm^2. *Operando* quick-XAS spectra were averaged over 10 minutes acquisition time at each absorption edge, with one hour between two consecutive acquisitions on the same cell, as three different cells were recorded during the same experiment. We have used the electrochemical cell designed in LRCS Amiens[39], cycled in a voltage window of 2.0 – 4.3 V vs. Na^+/Na with a C-rate of C/7 (1 Na^+ in 7 h). Several *ex situ* samples recovered at different voltages vs. Na^+/Na, *i.e.*, at different states of charge or discharge of the sodium batteries, were also studied. XAS spectra at the Mn and V K-

edges were recorded by averaging over 10 minutes of acquisition time using a Si(111) quick-XAS monochromator with an oscillation frequency of 2 Hz. Thanks to the edge-jump acquisition available at ROCK beamline, we have used three ionization chambers for the V and three others for the Mn K-edge measurements. V and Mn foils were used for the energy calibration and they were placed between the second (up and down) and the third (up and down) ionization chambers. The oxidation states of manganese and vanadium were deduced by the edge positions taken at the normalized absorption of 1. The analyses were performed with Athena and Artemis from the Demeter software package.[40] For the Extended X-ray Absorption Fine Structure (EXAFS) analysis, Fourier transforms of the k^2-weighted EXAFS oscillations for Mn and V K-edges were carried out in the k-range of 2.3 - 11.3 $Å^{-1}$ and 2.7 - 10.7 $Å^{-1}$, respectively. Fitting both Mn and V K-edges was performed within the R range of 1.0 - 2.1 Å, dR = 0 with sine window and the coordination number (N) of 6. Attenuation factors (S_0^2) for Mn and V K-edges were set as 0.887 and 0.884, respectively. The radial distance (R_i) and the Debye-Waller factor (σ_i^2) were refined while the energy shift (E_0) was refined at the beginning and then fixed in the last step.

Results and Discussion

Characterization of the pristine $Na_4MnV(PO_4)_3$ material

The positive electrode material $Na_4MnV(PO_4)_3$ was prepared by a sol-gel assisted method and the resulting powder had primary particles of few hundreds of nanometers size forming agglomerates ranging from several to tens of micrometers (**Figure S1**). As citric acid was used as a chelating agent and carbon source during the synthesis, carbon was coated on the surface of the particles. The amount of carbon coating was shown to be around 12.3 wt.% according to TGA analyses shown in **Figure S2a**. Numerous NASICON-type materials undergo a phase transition depending on the temperature, but $Na_4MnV(PO_4)_3$ showed no phase transition between -25 and 200 °C (**Figure S2b**). The Na/Mn/V/P ratio determined by ICP-OES analysis is 4.10(4):1.00(5):0.99(3):2.91(6) in a good agreement with the target composition 4:1:1:3.

The structural model of $Na_4MnV(PO_4)_3$ was determined with the Rietveld refinement of the SXRPD pattern as shown in **Figure 1**. $Na_4MnV(PO_4)_3$ crystallizes in the space group (*R*-3*c*) for NASICON-type materials with the refined cell parameters of *a* = 8.9640(2) Å, *c* = 21.4724(3) Å and *V*/*Z* = 249.034(4) Å^3. The obtained powder shows high purity, containing only 0.4(2) wt.% of $NaMnPO_4$ as a secondary phase, based on the results of Rietveld refinement (inset image of **Figure 1**). $NaMnPO_4$ is a common impurity encountered for $Na_4MnV(PO_4)_3$ preparation but its amount ranges typically from 0 to 3 wt.% depending on the synthesis conditions.[19,41–44] The occupancy factors of the Na(1) and Na(2) sites are both close to 1, i.e. 0.97(3) and 0.96(2), respectively, resulting in the $Na_{3.85(9)}MnV(PO_4)_3$ global composition. The detailed structural parameters of pristine $Na_4MnV(PO_4)_3$ are summarized in **Table S1**.

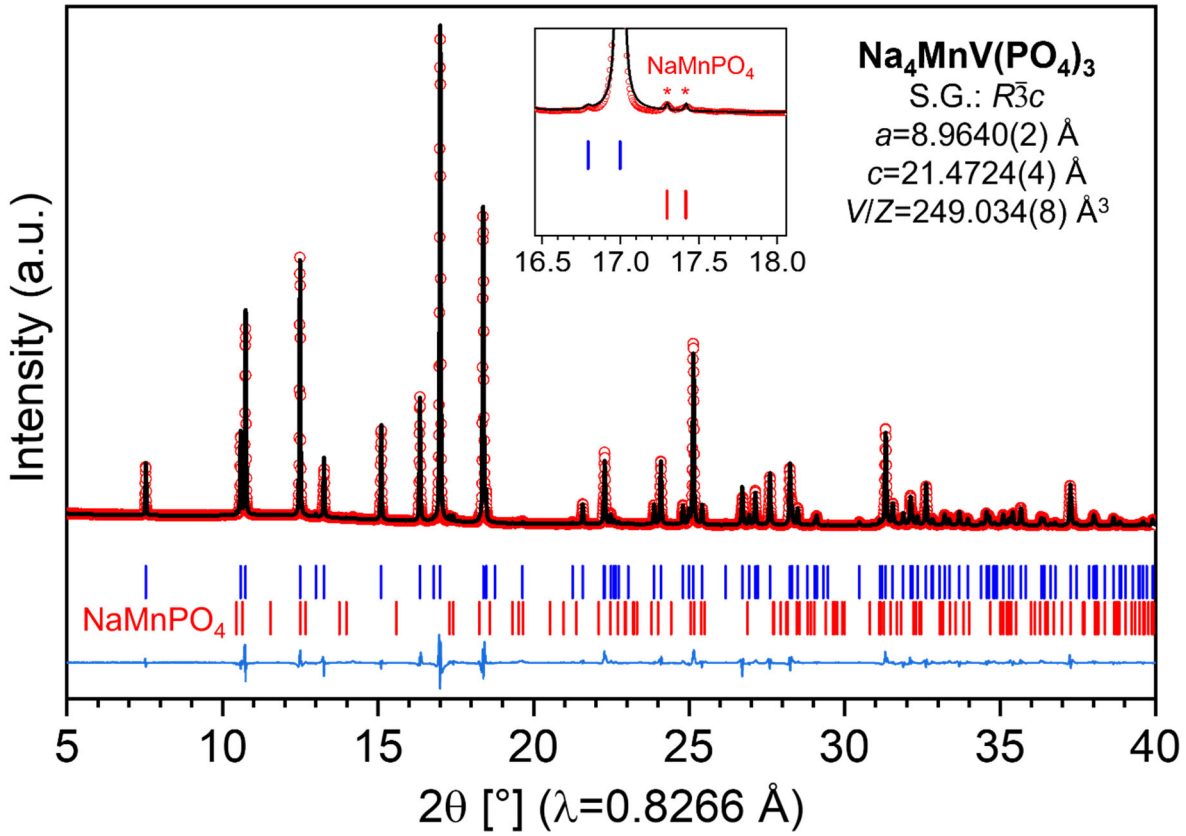

Figure 1. Rietveld refinement profile of the SXRPD pattern for $Na_4MnV(PO_4)_3$ powder.

Electrochemical properties and structural characterizations with different voltage windows

The electrochemical performance of $Na_4MnV(PO_4)_3$ as a positive electrode material was examined in half cells versus Na metal in different voltage windows. The galvanostatic voltage-composition data obtained during the first charge and discharge cycle in the voltage windows of i) OCV➔3.75V➔2V (hereafter referred as 2-3.75 V), ii) OCV➔4.3V➔2V (hereafter referred as 2-4.3 V), and iii) OCV➔4.3V➔1V vs. Na^+/Na (hereafter referred as 1-4.3 V) at the C-rate of C/10 (1 Na^+ in 10 h) are compared in **Figures 2a-c**.

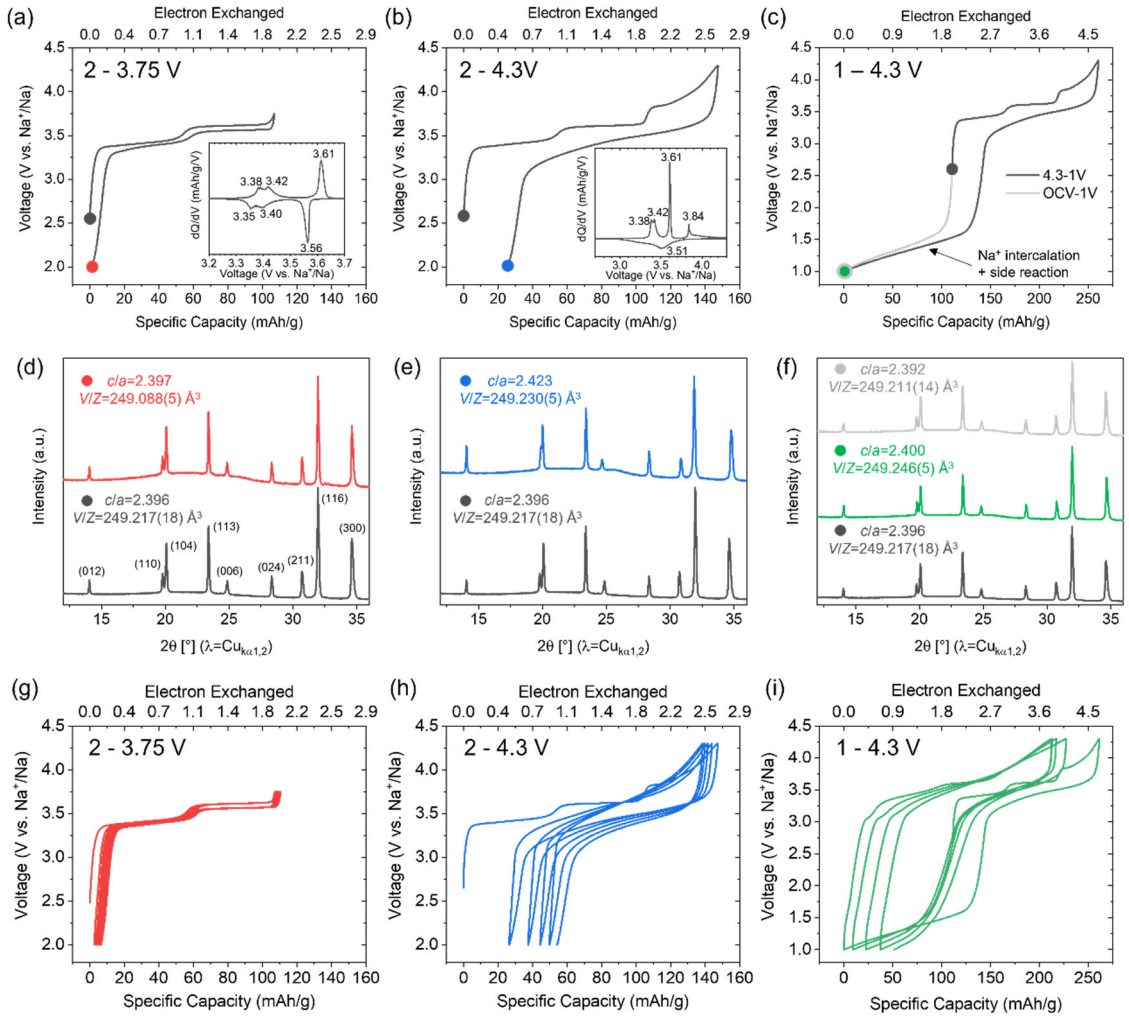

Figure 2. Electrochemical curves of $Na_4MnV(PO_4)_3$ cycled in half cells vs. Na metal within the voltage windows of **(a)** 2-3.75 V, **(b)** 2-4.3 V, **(c)** 1-4.3 V and OCV-1 V, during the first cycle. **(d-f)** The corresponding XRPD patterns of pristine material and those recovered after the different cycling conditions. **(g-i)** The corresponding charge discharge curves for the first 5 cycles. The upper y-axis is given in number of electrons exchanged and not in composition in Na^+ as parasitic degradation reactions occur especially in the potential window 1 - 4.3V, the number of electrons exchanged being thus not only associated to the active material itself.

When the first 2 Na^+ are extracted from the pristine material, up to 3.75 V, the electrochemical reaction is highly reversible (**Figure 2a**). Overall, two main voltage domains can be observed at ~3.4 and 3.6 V but the first plateau at 3.4 V is actually made of two successive domains, as highlighted by the two separated peaks at 3.38 and 3.42 V in the derivative curve (inset of **Figure 2a**) which suggests the existence of an intermediate $Na_{3.5}MnV(PO_4)_3$ composition. When extending the upper cut-off voltage to 4.3 V, about 2.7 Na^+ are extracted, with an additional voltage domain at 3.84 V (**Figure 2b**). However, severe irreversibility was observed in the following discharge, with a modified electrochemical mechanism as suggested by the S-shaped sloping curve and only ~2.2 Na^+ can be re-inserted. The same phenomenon was reported in other studies of $Na_4MnV(PO_4)_3$ when more than 2 Na^+ are extracted.[18–20,23] Interestingly, the irreversibility due to the activation of $V^{5+/4+}$ redox couple can be partially retrieved by over-discharging to a very low voltage, down to 1 V vs. Na (**Figure 2c**) as also observed in other V-containing NASICON materials.[34,45] With this strategy, about 0.5 Na^+ can be further recovered but the intercalation proceeds concomitantly with the side reaction originated from the conductive carbon with the electrolyte.[13,46] The contribution from the side reaction can also be evidenced when a pristine electrode (with fully occupied Na sites) is directly discharged to 1 V (**Figure 2c**): the electrochemical reaction does not come from Na^+ intercalation as there is no site for Na^+ insertion. Nevertheless, the over-discharge cannot prevent a rapid capacity fading with the extended upper cut-off voltage utilizing the activation of $V^{5+/4+}$ redox couple (**Figure 2i**). The electrochemical performance of $Na_4MnV(PO_4)_3$ for the first 5-20 cycles upon three different voltage windows are shown in **Figure S3**.

To analyze the structural evolutions depending on the voltage windows, XRPD patterns collected at OCV and after the first cycle within the three different voltage windows are compared in **Figures 2d-f**. As expected from the electrochemical data, operating the battery within the voltage window of 2 - 3.75 V allows reversible Na^+ extraction/insertion resulting in very similar cell parameters and Na^+ occupancy ratios before and after cycling, as summarized in **Table 1**. On the contrary, in the case of the voltage window of 2 - 4.3 V, a contracted *a* parameter, an elongated *c* parameter and, importantly, a much decreased Na^+ occupancy were found after the first cycle,

compared to those from pristine materials: *a* = 8.9324(2) Å, *c* = 21.6413(3) Å (thus *c*/*a* = 2.423), and 3.50(5) Na^+ per formula unit [Na(1) = 0.89(3), and Na(2) = 0.871(6)]. The change in the *c* parameter was more pronounced than that of the *a* parameter mainly because the increased *c* parameter is closely related to the depopulation of the Na(1) site [12,47,48]. The positions of the (110) and (104) reflections, for instance, are also noticeably shifted after the first cycle (**Figure 2e**). Interestingly, once the $Na_4MnV(PO_4)_3$ electrode is over-discharged down to 1 V after being charged up to 4.3 V, the irreversible structural modification is mostly restored, with cell parameters and Na^+ occupancy similar to those of the pristine material. When the pristine electrode is directly discharged to 1 V (*i.e.*, OCV-1 V), the cell parameters and the Na^+ occupancy factors are barely changed, suggesting that the electrochemical reaction is mainly due to the side reaction described above.

Table 1. Unit cell parameters, volume per formula unit (*V*/*Z*) and Na site occupancy for $Na_xMnV(PO_4)_3$ compositions. The structures are described in the *R*-3*c* space group and were determined from the Rietveld refinement of *ex situ* XRPD patterns collected for the pristine material and those recovered after the first cycle within different voltage windows.

Cycling condition	*a* (Å)	*c* (Å)	*c*/*a*	*V*/*Z* (Å^3)	Na(1) Occ.	Na(2) Occ.	Total Na /f.u.
Pristine	8.9652(3)	21.4824(10)	2.396	249.217(18)	0.95(4)	0.973(13)	3.87(7)
2 - 3.75 V	8.9632(2)	21.4805(7)	2.397	249.088(5)	0.93(2)	0.938(7)	3.74(4)
2 - 4.3 V	8.9324(2)	21.6413(3)	2.423	249.230(5)	0.89(3)	0.871(6)	3.50(5)
1 - 4.3 V	8.9609(2)	21.5053(3)	2.400	249.246(5)	1.00(3)	0.958(14)	3.87(7)
OCV - 1 V	8.9698(3)	21.4594(8)	2.392	249.211(14)	0.97(3)	0.968(9)	3.88(5)

XAS spectra at Mn and V K-edges were acquired to assess the oxidation states and local environments of Mn and V in $Na_4MnV(PO_4)_3$ at different voltage windows. X-ray Absorption Near-Edge Structure (XANES) spectra at Mn and V K-edges are compared within the three different voltage windows before and after battery operation (charge + discharge) in **Figure 3a-b**. At the Mn K-edge, the XANES spectra of the pristine material and of the electrode recovered after one cycle within the voltage window of 2 - 3.75 V, are very similar. On the contrary, for the material recovered after one cycle within the voltage window 2 - 4.3 V, although the edge position is almost the same as that of the pristine one, the oscillations observed in the post-edge region become

smoother. These smoothed oscillations are partially restored in the XANES spectrum of the sample cycled between 1 and 4.3 V. The V K-edge XANES spectra show globally the same trend as those at the Mn K-edge, but with a much more pronounced pre-edge when the electrode was cycled between 2 and 4.3 V. The increased intensity of the pre-edge gives a clear evidence of an irreversible modification of the vanadium local environment, the centrosymmetric environment becoming more asymmetric.[49] In the case of the sample directly discharged to 1V, the XANES spectra of both Mn and V K-edges barely changed compared to those of the pristine $Na_4MnV(PO_4)_3$, confirming that the corresponding electrochemical activity results from the side reaction with the carbon additive and the electrolyte.

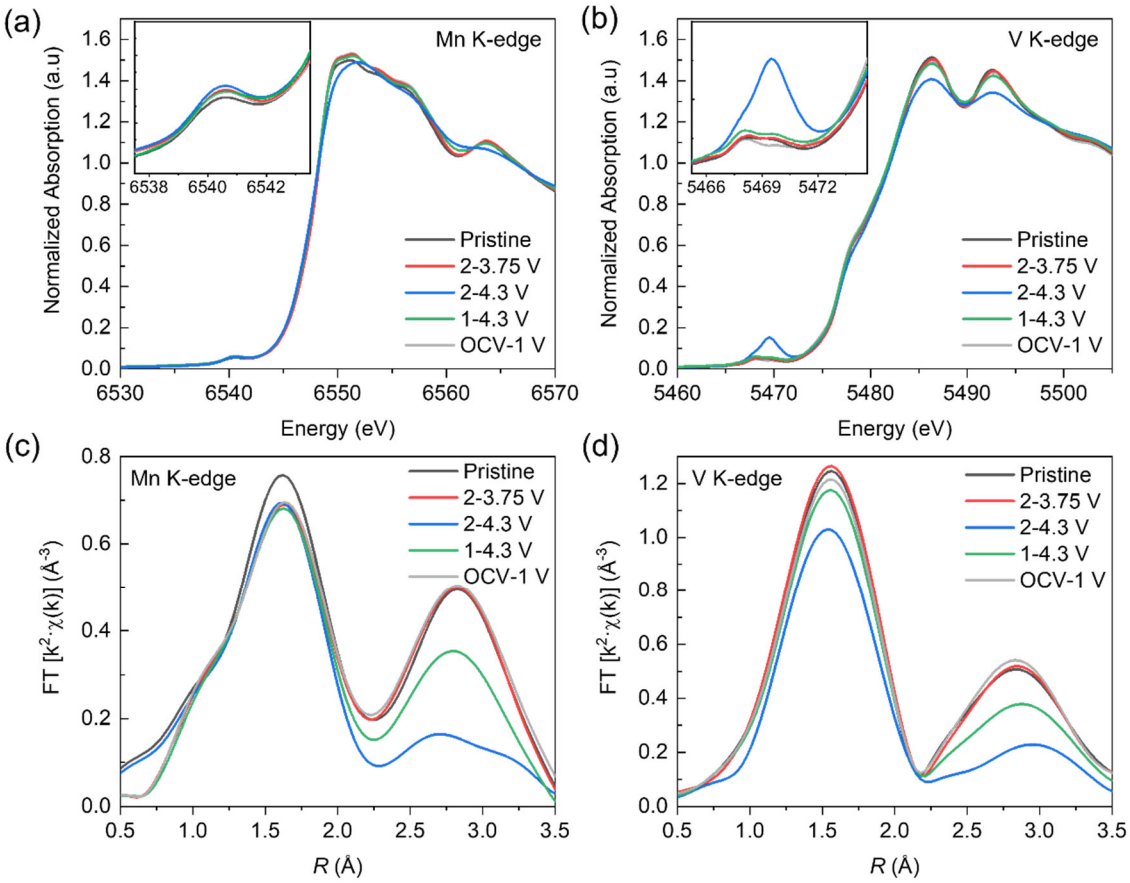

Figure 3. XAS of $Na_4MnV(PO_4)_3$ recovered after first charge and discharge cycles performed within different voltage windows. The XANES spectra at **(a)** Mn K-edge and **(b)** V K-edge. Fourier transform of the EXAFS spectra at **(c)** Mn K-edge and **(d)** V K-edge.

Extended X-ray Absorption Fine Structure (EXAFS) analysis was carried out for quantitative understanding of local environments of Mn and V. **Table 2** shows the

refined Mn-O and V-O distances in the first coordination shells after batteries were charged and discharged in different voltage windows during the first cycle (**Figures 2a-c**). After 2 Na^+ extraction/insertion sequences, the Mn-O distance does not change significantly, confirming also the high reversibility of the reaction around the Mn site at the local scale. On the contrary, when more than 2 Na^+ are extracted, the Mn-O distance decreases from 2.138(5) to 2.122(5) Å, and it recovers to 2.133(5) Å only after the deep discharge down to 1 V. The first coordination shell of vanadium requires to be described by a single V-O scattering path with very similar bond lengths for all samples, except for the one recovered after one cycle between 2 and 4.3 V (**Table 2**). After the $V^{5+/4+}$ redox couple is activated, ~0.4 Na^+ was not re-inserted in the structure, meaning that unreduced transition metals including a vanadyl-type bond in their first coordination shell exist at 2.0 V after the first cycle. The intensity of the pre-edge peak of the XANES spectrum dramatically increases at the V K-edge, indicating vanadium environments being distorted and non-centrosymmetric.[23,31,34,49,50] The edge position is also slightly shifted toward higher energy from 5841.9 to 5842 eV. Note that the edge shift due to the oxidation/reduction of the vanadyl bond is relatively small compared to that observed for regular vanadium-oxygen bond,[49] thus the amount of unreduced vanadium may be greater than what is suggested by the edge shift. Therefore, an adequate model with a coordination shell involving 5.5 regular V-O bonds of 2.013(5) Å and 0.5 short V – O bond of 1.645(5) Å, was introduced to describe the combined symmetric and more distorted environments for the EXAFS spectrum of V K-edge recovered after one cycle between 2 and 4.3 V. The detailed of the fit for the 5.5+0.5 model is displayed and compared with 6 model in **Figure S4** and **Table S2**.

Similarly, for the second shells observed at both Mn and V K-edges, when the voltage window is extended up to 4.3 V, the local structure changes after cycling, and deep-discharging down to 1 V allows partial recovery. Note that the second coordination shell overlaps multiple scattering paths, such as single scattering of M-Na (M= Mn or V) and M-P and multi scattering of M-O-P as shown in **FIgure S5**. It is thus difficult to distinguish the influence of each path on the local structure, but the structure contains more disordered environments as the amplitude of the second shell decreases.

Table 2. Mn-O and V-O distances in the first coordination shells, by fitting the EXAFS oscillations collected at Mn and V K-edges, for $Na_4MnV(PO_4)_3$ recovered after first charge and discharge cycles performed within different voltage windows. E_0 values are refined between -0.1 and 1.8 eV.

Cycling condition	N	σ^2 (Å^2)	R-factor	Mn-O (Å)	N	σ^2 (Å^2)	R-factor	V-O (Å)
Pristine	6	0.0100	0.0126	2.138(5)	6	0.0051	0.0033	2.019(5)
2 - 3.75 V	6	0.0107	0.0130	2.137(5)	6	0.0045	0.0027	2.019(5)
2 - 4.3 V	6	0.0100	0.0023	2.122(5)	5.5 0.5	0.0058	0.0017	2.013(5) 1.645(5)
1 - 4.3 V	6	0.0110	0.0117	2.133(5)	6	0.0053	0.0023	2.020(5)
OCV - 1 V	6	0.0106	0.0147	2.139(5)	6	0.0050	0.0020	2.021(5)

Long-range structural evolution upon Na^+ extraction / insertion

To characterize the structural evolution during charge and discharge, *operando* SXRPD experiments were performed with a cell cycled between 1 and 4.3 V vs. Na^+/Na at a C-rate of C/9 (1 Na^+ in 9 h), as shown in **Figure 4**. Wider 2θ range (2θ = 5-30°) of the set of the SXRPD patterns can be found in **Figure S6**. The corresponding unit cell volume (*V*/*Z*) evolution is presented in **Figure 5** as a function of the state of charge and discharge.

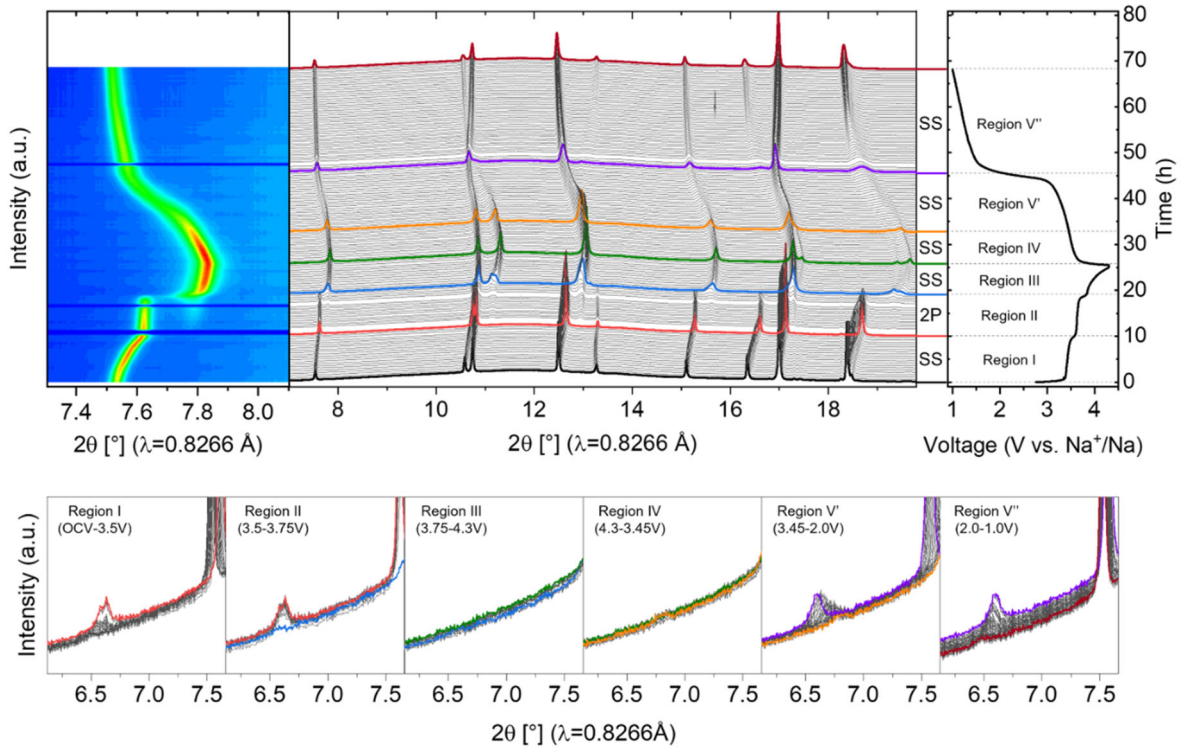

Figure 4. (top) *Operando* SXRPD measurement during the first charge and discharge cycle of $Na_4MnV(PO_4)_3$ vs. Na metal within the voltage window of 1.0 - 4.3 V vs. Na^+/Na at a C-rate of C/9 (1 Na^+ in 9 h). SS and 2P indicate solid-solution and two-phase reactions, respectively. (bottom) Enlarged view of the SXRPD patterns in the 6.1 - 7.7 ° 2θ range.

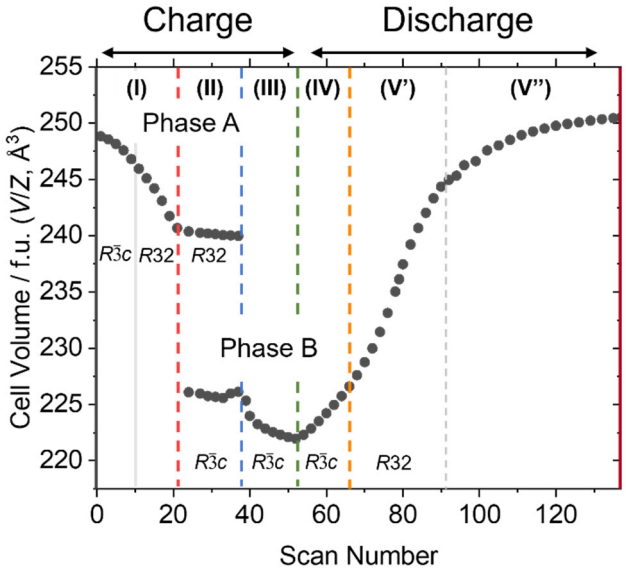

Figure 5. Evolution of the unit cell volume per formula unit (*V*/*Z*) obtained from the *operando* SXRPD measurement. The SXRPD patterns in region V'' were refined using the *R*-3*c* space group for comparison purpose. Note that the SXRPD pattern was recorded every ~30 minutes.

The successive mechanisms involved upon Na^+ de-intercalation up to 4.3 V and re-intercalation down to 1 V occur through i) a solid solution reaction (region I), ii) a two phase reaction (region II) and iii) a solid solution reaction (region III) during charge, while a complete solid solution reaction is observed during discharge (regions IV and V). From $Na_4MnV(PO_4)_3$ to $Na_3MnV(PO_4)_3$, the first Na^+ is extracted through a solid solution mechanism as observed for other Na_4-type NASICON compounds such as for the MnCr[27,29] and the FeV[13–15,49] systems. It is interesting to point out that two diffraction reflections start appearing at ~6.6° from the $Na_{3.5}MnV(PO_4)_3$ composition, and their intensities evolve until the $Na_3MnV(PO_4)_3$ composition (**Figure S7**). In the case of the FeV system, a monoclinic distortion (associated to a superstructure due to Na^+ ordering) described with the *C*2/*c* space group was confirmed for the $Na_3FeV(PO_4)_3$ composition.[13] Zakharkin *et al.*[19] described the structure of $Na_3MnV(PO_4)_3$ using the *C*2/*c* space group, a typical space group for NASICON-type materials.[3–5] However, as a result of our detailed examination, two diffraction peaks were observed at 6.58° and 6.63° and only the former reflection could be explained using the *C*2/*c* space group (inset **Figure S7**). Our new structural model for $Na_3MnV(PO_4)_3$, therefore, uses the *R*32 space group which can successfully explain the presence of two reflections at low angle (**Figure 6**a). The refined structural parameters are summarized in

Table 3.

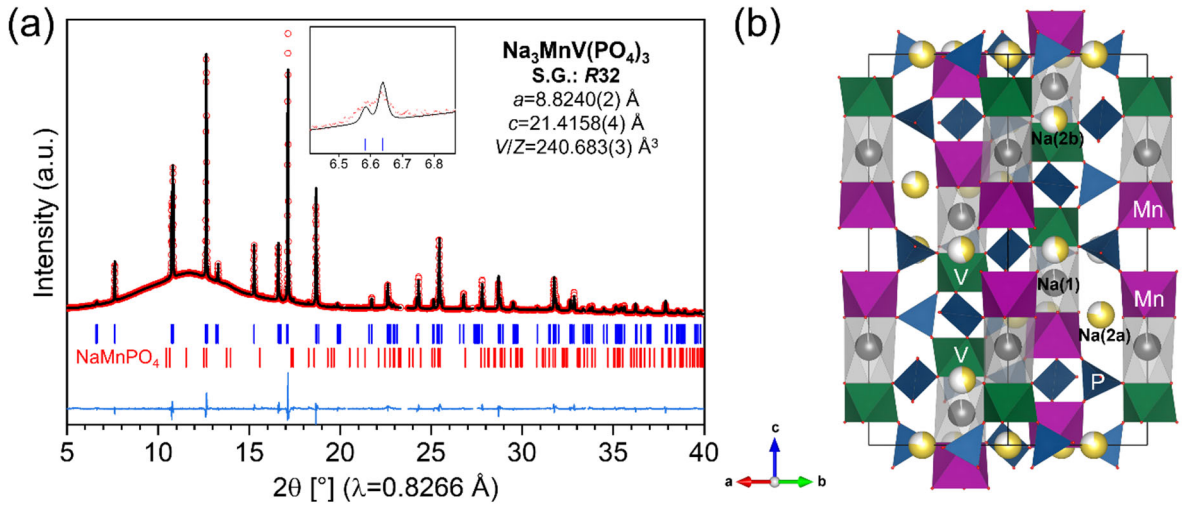

Figure 6. **(a)** Rietveld refinement profile and **(b)** corresponding crystal structure (described in the R32 space group) of $Na_3MnV(PO_4)_3$, obtained from the analysis of the SXRPD pattern collected with the *in situ* cell during charge.

Generally, the *R*32 space group can be used for NASICON-type structures when cation ordering occurs at the transition metal site.[3,51] In the case of $Na_4AlMn(PO_4)_3$ described with the *R*32 space group, the large difference in the ionic radii of Al^{3+} (0.675 Å) and Mn^{2+} (0.97 Å) is foreseen as the cause of cation ordering.[51] For the MnV system, the difference in ionic radii between vanadium ions and Mn^{2+} (0.97 Å) becomes greater as V^{3+} (0.78 Å) is oxidized to V^{4+} (0.72 Å). As a result, the metal site is split into two distinct positions with a symmetry and multiplicity reduction (from one 12*c* Wyckoff site to two 6*c* Wyckoff sites). As can be seen from the illustration of the structure, each of the Mn and V atoms form respective $Mn_2(PO_4)_3$ and $V_2(PO_4)_3$ lantern units (**Figure 6b**). This suggests that the distribution of Mn and V in the pristine state is also ordered, but it was difficult to confirm it based on the results of X-ray diffraction only. Neutron diffraction as complementary characterization will be helpful to further confirm this.

Table 3. Refined structural parameters of the $Na_3MnV(PO_4)_3$ phase from the SXRPD pattern collected with the *in situ* cell during charge.

$Na_3MnV(PO_4)_3$

Space group: *R*32 (#155); *Z* =6

a = 8.8240(2) Å; *c* = 21.4158(2) Å; *c*/*a* = 2.427

V= 1444.099(18) Å^3; *V*/*Z*=240.683(3) Å^3

R_{wp} = 14.1 %; R_p = 19.0 %; R_{Bragg} = 5.5 %

Atom	Wyckoff position	*x*/*a*	*y*/*b*	*z*/*c*	Uiso, Å^2	Occ.
Mn	6*c*	0	0	0.6007(9)	0.034(7)	1
V	6*c*	0	0	0.8996(9)	0.022(6)	1
P(1)	9*d*	0.7144(18)	0	0	0.023(2)	1
P(2)	9*e*	0.3070(17)	0	0.5	0.023(2)	1
Na(1)	6*c*	0	0	0.748(3)	0.038(8)	0.98(3)
Na(2a)	9*d*	0.384(4)	0	0	0.034(10)	0.77(5)
Na(2b)	9*e*	0.662(6)	0	0.5	0.034(10)	0.44(5)
O(1a)	18*f*	-0.0171(9)	0.194(3)	0.4442(10)	0.023(3)	1
O(1b)	18*f*	0.959(2)	0.787(3)	0.0587(9)	0.023(3)	1
O(2a)	18*f*	0.197(2)	0.174(3)	0.3267(11)	0.023(3)	1
O(2b)	18*f*	0.827(3)	0.828(3)	0.1584(11)	0.023(3)	1

From Na_3 to Na_2 compositions, a phase transition occurs (phase A → phase B). The volume contraction during the phase transition is about -5.8 %, which is much higher than for the FeV system ($\Delta V/V$ = -1.8 %).[49] The difference in ionic radii between V^{4+} (0.72 Å) and Mn is greatly reduced as Mn^{2+} (0.97 Å) is oxidized to Mn^{3+} (0.785 Å) and therefore, one crystallographically independent position for the metal site is sufficient to describe the structure. This is further confirmed by the fact that no reflection at around 6.5° was observed for phase B. Thus, it can be described with the *R*-3*c* space group until the end of charge (**Figure 5**). By extending the upper-cut off voltage to 4.3 V (region III), the third Na^+ extraction (Na_2 – $Na_{1.3}$) is possible and the reaction proceeds according to a solid solution mechanism.

Table 4. Space group (S.G.), unit cell parameters, *V*/*Z* value, Na site occupancy factors and average M-O distance (M = Mn, V) determined from the Rietveld refinement of the SXRPD patterns collected *operando* at different states of charge.

	Voltage	S.G.	*a* (Å)	*c* (Å)	*c*/*a*	*V*/*Z* (Å^3)	Na(1) Occ.	Na(2) Occ.	Total Na /f.u.	Avg. M-O (Å)
$Na_4MnV(PO_4)_3$	OCV	*R*-3*c*	8.9626(2)	21.4615(2)	2.395	248.833(3)	0.98(3)	0.953(16)	3.84(7)	2.096(10)
$Na_3MnV(PO_4)_3$	3.5V	*R*32	8.8240(2)	21.4158(2)	2.427	240.683(3)	0.98(3)	0.61(5)	2.80(17)	1.990(13) / 2.121(14)
$Na_{2.08}MnV(PO_4)_3$	3.75V	*R*-3*c*	8.5438(3)	21.6693(12)	2.536	228.308(16)	0.96(6)	0.30(3)	1.87(15)	1.96(2)
$Na_{1.3}MnV(PO_4)_3$	4.3V	*R*-3*c*	8.3840(2)	21.8774(8)	2.609	221.962(10)	0.71(3)	0.20(2)	1.30(10)	1.90(3)

During the full charge process between the compositions Na_4 and $Na_{1.3}$, a global volume change of about -10.8 % was therefore observed (**Table 4**), which is similar to the previously reported studies[18,19] (for comparison, *V*/*Z* = -7.3 % between $Na_4FeV(PO_4)_3$ and $Na_{1.3}FeV(PO_4)_3$ [49]). For Na^+ occupancy factors, the Na(1) site is almost fully occupied while the Na(2) site is gradually depopulated during the first two Na^+ extraction (regions I and II). However, during the third Na^+ extraction (region III), sodium is extracted from both Na(1) and Na(2) sites. As Na^+ is removed from the Na(1) site, the *c* parameter begins to increase rapidly due to stronger repulsion of oxygen atoms along the c_{hex} direction.[12,47,48] A very similar trend was also observed in other NASICON-type materials when the high voltage domain (*i.e.*, the activation of $V^{5+/4+}$ redox couple) is involved.[14,18,19,45] The metal-oxygen distance also gradually decreased from 2.096(10) to 1.90(3) Å during the charge process (**Figure 7**). As mentioned above, when phase A reached the $Na_{3.5}$ composition, two M–O distances appeared, and reached the Mn-O distance of 2.121(14) Å and the V-O distance of 1.990(13) Å in the $Na_3MnV(PO_4)_3$ composition. This is in good agreement with *operando* XAS data, which will be described later.

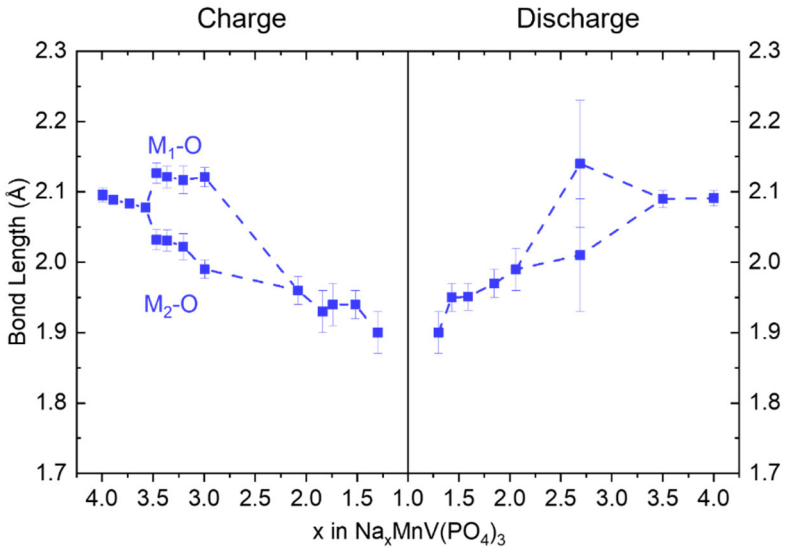

Figure 7. Evolution of the metal-oxygen distances obtained from the Rietveld refinements of the SXRPD patterns collected for $Na_xMnV(PO_4)_3$ during the first charge and discharge. The data points for $Na_{3.5}MnV(PO_4)_3$ and $Na_4MnV(PO_4)_3$ compositions during discharge are from Figures 2d-f.

During the discharge process, the voltage plateaus observed during charge disappear and the electrochemical reaction occurs through a full solid solution mechanism. From $Na_{1.3}$ to Na_2 composition (region IV) the reflection at ~6.6° is not observed, the structure is thus described with the *R*-3*c* space group. Furthermore, the sodium occupancy ratio of the Na(1) site in $Na_{1.85}MnV(PO_4)_3$, obtained in discharge during re-sodiation, is 0.82(6) which is much more depopulated compared to the Na(1) site for the same composition during charge [0.96(6)]. When the discharge process continues to 2.0 V (Region V'), a $Na_{3.5}$ composition is reached. When the cut-off voltage is lowered to 1 V (region V''), 0.5 Na^+ is further intercalated in the structure. A partial recovery of the irreversible structural transformation proceeds gradually with side reaction while the voltage decreases to 1 V.

Evolutions of oxidation states and local environments of Mn and V upon cycling

To investigate the redox mechanism and the local environments of Mn and V in $Na_xMnV(PO_4)_3$ at different states of charge and discharge of the battery, X-ray absorption spectroscopy experiments were performed *ex situ* and *operando*. **Figure 8** shows the *operando* XANES spectra at Mn and V K-edges, when the cell was cycled between 2.0 and 4.3 V versus Na metal at the C-rate of C/7 (1 Na^+ in 7 h). The

evolution of their edge position (taken at the normalized absorption of 1) is summarized in **Figure 9**. The data points of the XAS spectra and the voltage profile obtained with the *in situ* cell for the XAS *operando* measurements are shown in **Figure S8**. When the first Na^+ is extracted (region I), the V edge position is shifted to higher energy, indicating that V^{3+} is oxidized to V^{4+}. On the other hand, the Mn edge position barely shifts, but the shape of the spectra after the edge is modified. This means that the removal of Na^+ together with the oxidation of V^{3+} to V^{4+} affects the Mn local environment. Such modifications of the XAS spectra of elements which are not involved in the redox reaction were also observed in other studies.[49,52,53] When the second Na^+ is extracted (region II), we expect a gradual shift of the edge towards higher energy as Mn^{2+} is oxidized to Mn^{3+}. However, the edges moved abruptly at the end of the extraction of the second Na^+, suggesting a cooperative Jahn-Teller effect of the Mn^{3+} involved in the Mn^{2+}/Mn^{3+} reaction. In the region III, where the third Na^+ is extracted, the trace of remaining un-oxidized manganese is fully oxidized to Mn^{3+}, while the V K-edge slightly shifts, but the intensity of the pre-edge peak severely increases, which is the evidence of V^{5+} in NASICON-type materials.[49,50] Note that the oxidation states of Mn and V in $Na_xMnV(PO_4)_3$ are deduced from the edge positions of the reference samples ($Mn^{2+}SO_4$, $Mn^{3+}OOH$, $Na_3V^{3+}{}_2(PO_4)_3$, and $Na_1V^{4+}{}_2(PO_4)_3$). We could not find a reference with pure V^{5+} in symmetric oxygen octahedral environment as expected in $Na_1MnV(PO_4)_3$, the six oxygen anions being involved in antagonist covalent X-O bonds (X = P, S etc.). Indeed, that environment is very different from those observed in $VOPO_4$ in which V^{5+} cations are involved in highly covalent vanadyl type bonds (as tentatively highlighted in **Figure S9**).

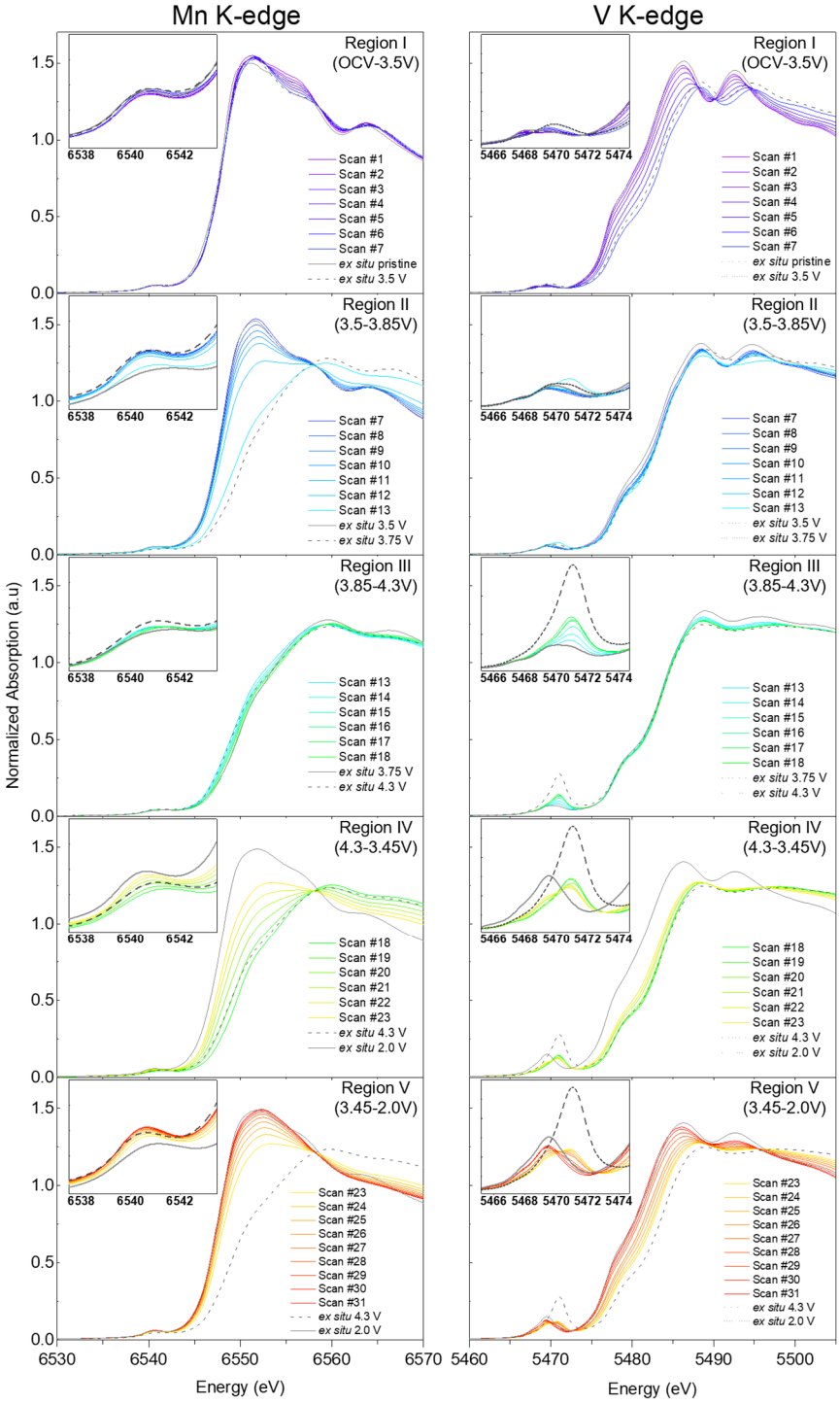

Figure 8. *Operando* XANES spectra at Mn and V K-edges collected during the first cycle of $Na_4MnV(PO_4)_3$ vs. Na metal within a voltage window of 2.0 - 4.3 V at a C-rate of C/7 (1 Na^+ in 7 h).

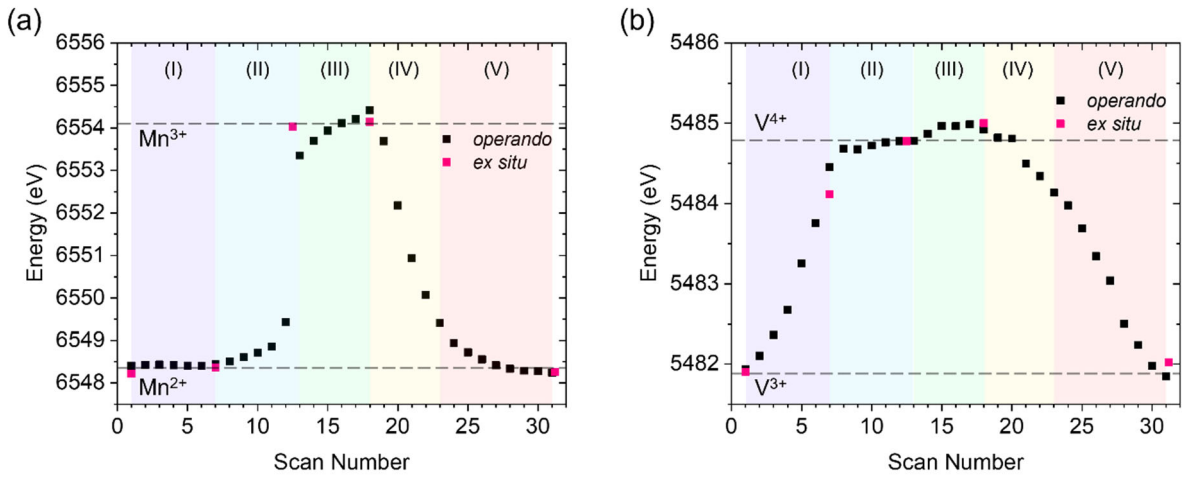

Figure 9. Evolution of the edge positions of **(a)** Mn and **(b)** V K-edges during the *operando* XAS measurement. The edge energy values are taken at the normalized absorption of 1. The dashed lines indicate the edge energies of the references: $Mn^{2+}SO_4$, $Mn^{3+}OOH$, $Na_3V^{3+}{}_2(PO_4)_3$, $Na_1V^{4+}{}_2(PO_4)_3$.

During discharge, both manganese and vanadium are gradually and simultaneously reduced, *i.e.*, without the activation of respective redox centers for each domain. Although the edge shift does not simply match with the oxidation state in some cases, as can be seen from the edge shifts of $V^{3+} \rightarrow V^{4+}$ compared to $V^{4+} \rightarrow V^{5+}$, the overall trends of the oxidation states of Mn and V are tracked based on the edge positions. When the battery is discharged from 4.3 to 3.45 V most of manganese ions are reduced as the average oxidation state is about $Mn^{2.2+}$, while only a small amount of vanadium ions is reduced reaching the average oxidation state of about $V^{3.8+}$. As the discharge process continues to 2.0 V, Mn and V are entirely reduced to Mn^{2+} and V^{3+}, respectively, but the intensity of the pre-edge for V K-edge still remains prominent.

Figure 10 shows the Fourier transforms (FT) of the EXAFS oscillations extracted at Mn and V K-edges collected in *operando* conditions. **Figure 11**, **Table S3** and **Table S4** indicate the Mn–O and V–O distances in their first coordination shells in $Na_xMnV(PO_4)_3$ recovered at different states of charge and discharge. Overall, the metal-oxygen distance obtained from XRD analysis is in excellent agreement with the Mn-O and V-O distances resulting from the EXAFS analysis.

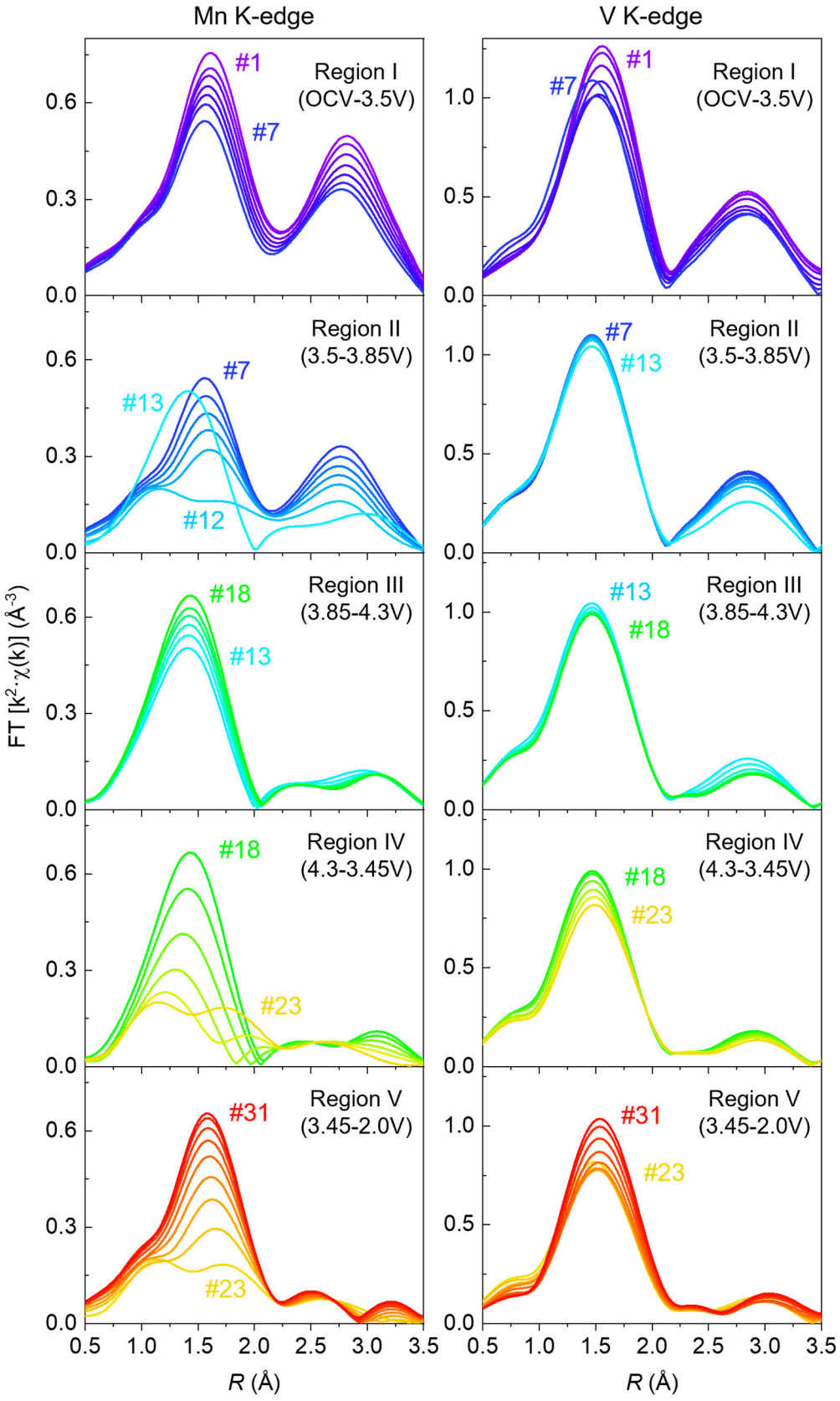

Figure 10. Fourier transforms of the EXAFS oscillations at Mn and V K-edges collected in *operando* conditions on $Na_4MnV(PO_4)_3$ positive electrode. The FTs are not corrected by the phase shifts. The EXAFS oscillations without FT is shown in Figure S10.

The first charge domain occurs through the $V^{4+/3+}$ redox couple, but the Mn-O distance also decreases slightly, which is in good agreement with the XANES analysis. In the second charge domain, the intensity of the main peak of the Fourier transforms obtained at Mn K-edge continues to decrease until scan #12. After that, the intensity increases until the end of charge (region III). Such drastic decrease (#12) and increase (#13) of the intensity reflects the occurrence of the Jahn-Teller distortion.[52] Very similar behavior was observed in $LiFe_{0.75}Mn_{0.25}PO_4$ when Mn^{2+} is oxidized to Mn^{3+} during charge, leading to elongated Mn^{3+} Jahn-Teller distortion.[52] In the third charge domain, we expect most of manganese ions in trivalent oxidation state and we obtain that the Mn-O equatorial distances are 1.926(5)-1.935(5) Å and the axial distances are of 2.240(5)-2.256(5) Å, in good agreement with an elongated Mn^{3+} Jahn-Teller distortion. The calculated structure of $Na_2MnV(PO_4)_3$ by DFT also shows Jahn-Teller distortion of Mn^{3+}, having axial bond distances of 2.24 and 2.31 Å with an average equatorial distance of 2.17 Å in MnO_6 octahedra.[21]

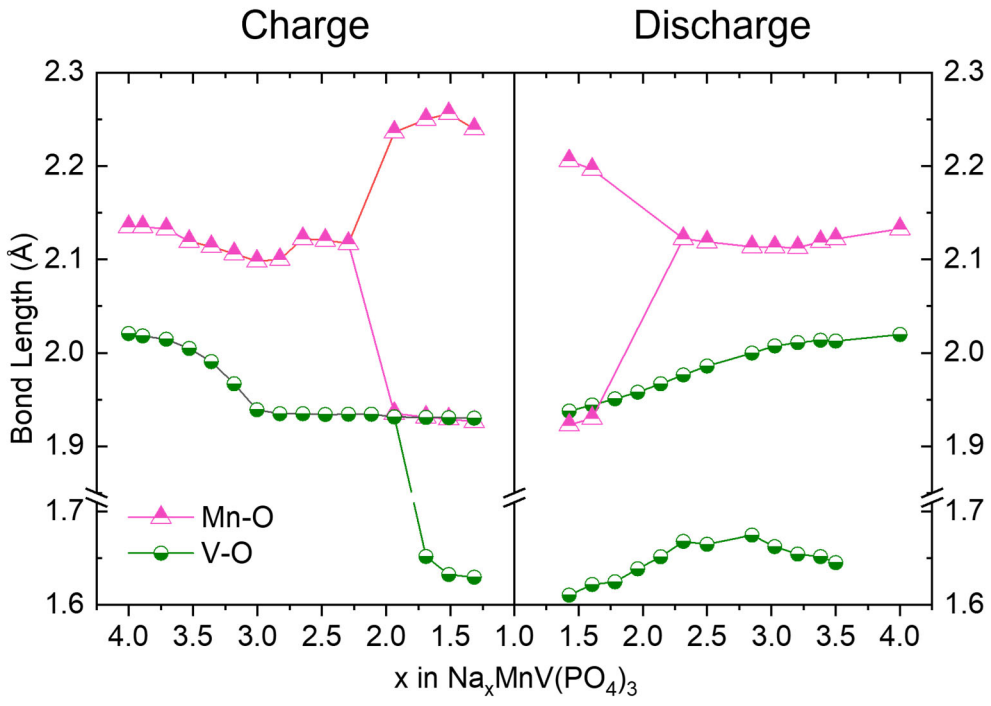

Figure 11. Mn-O and V-O bond lengths obtained from the EXAFS analysis on $Na_xMnV(PO_4)_3$

The distorted Mn environment recovers its symmetrical configuration over the discharge process. From 4.3 to 3.45 V, the intensity of the main peak of the FTs

decreases, scan #23 being similar to scan #12, and then its intensity increases back as it is further discharged down to 2.0 V. The Mn coordination shell changes from a [4+2] Mn-O environment to [6] Mn-O symmetric environment near the Na_2 composition.

The EXAFS oscillations extracted at V K-edge were also modeled in order to obtain information on the V-O bond length. In the first charge domain (region I), the V-O distance decreases from 2.021(5) to 1.939(5) Å, indicating that V^{3+} is oxidized to V^{4+}. In the second charge domain, it was on the contrary almost constant as varying in the range 1.939(5)-1.931(5) Å. In the third domain, the V-O length of the regular bond hardly changes over cycling, while a short V-O bond around 1.63 Å was required to describe the first coordination shell. The average V-O distance in the first coordination shell decreases from 1.931(5) to 1.916(5) Å in the third domain. During discharge down to 2 V, the regular V-O distance gradually increases from 1.930(5) to 2.013(5) Å, whereas the short V-O distance remains observed. However, this short V-O bond disappears as the electrode is over-discharged to 1.0 V (**Table 2**).

Ageing mechanism in $Na_4MnV(PO_4)_3$

After 5 cycles for the $Na_4MnV(PO_4)_3$ electrode in the voltage window of 2-4.3 V vs. Na^+/Na, the reversible capacity decreased sharply, resulting in re-sodiation limited to about 1.55 Na^+ (~86 mAh/g) as shown in **Figure 2h**.

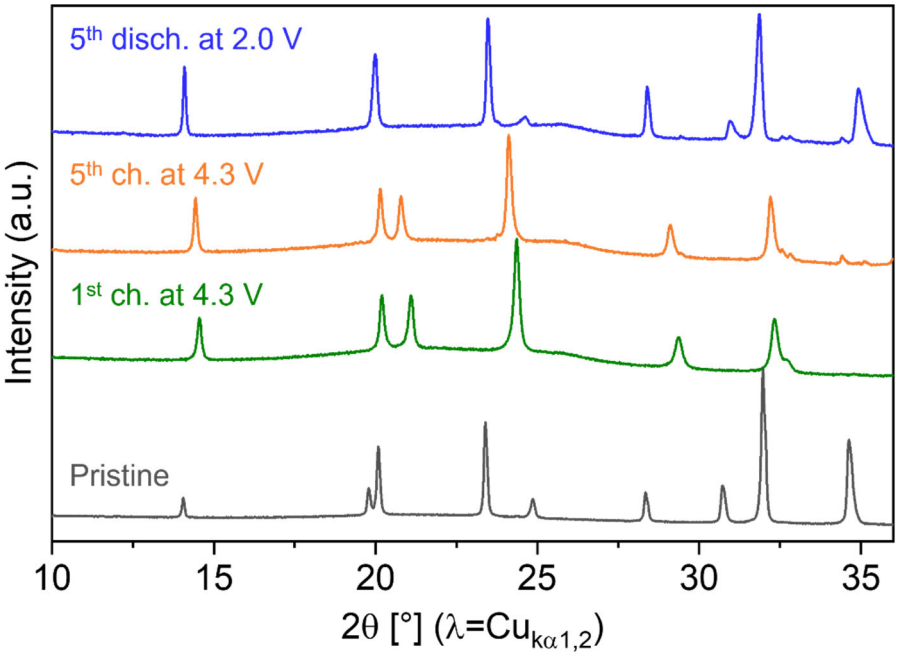

Figure 12. The XRPD patterns of the $Na_4MnV(PO_4)_3$ pristine material, the material recovered after the first charge, and the materials recovered after the fifth charge and the fifth discharge, when cycled between 2 and 4.3 V vs. Na^+/Na.

The XRPD patterns of $Na_4MnV(PO_4)_3$ after the fifth charge and discharge are compared in **Figure 12** with those of the pristine material and of the material recovered after the first charge. The corresponding cell parameters and Na^+ occupancy are summarized in **Table 5**. At the end of the first charge, it was found that the *c* parameter increased to 21.8774(8), and Na(1) site was depopulated down to 0.71(3). At the end of the fifth charge, the *c* parameter further increased to 21.9482(14) and the occupancy ratio of the Na(1) site decreased to 0.47(6). As the aging process progressed, less and less sodium ions occupy the Na(1) site. However, the total number of Na^+ per formula unit is about the same for both, *i.e.*, after the first and fifth charges. Thus, the Na(2) site is more populated for the fifth charged sample [0.28(2)] than for the first charged sample [0.20(2)].

At the end of the fifth discharge, the structure of the recovered material was investigated by full pattern matching data analysis only as a full crystal structure determination by the Rietveld method was not successful. The refined cell parameters are *a* = 8.9087(3) Å, *c* = 21.7102(13) Å, and *V*/*Z* = 248.70(2) $Å^3$ which means a significantly decreased *a* parameter, increased *c* parameter, and decreased cell

volume (*V*/*Z*) compared to those of pristine material (see **Table 5**). Na^+ distributions in the discharged state could be inferred based on the refined cell parameters. A decrease in volume implies a decrease in the number of Na^+ in the structure, and an increase in the *c* parameter indicates that the Na(1) site is depopulated.[12,47,48]

Table 5. Unit cell parameters, volumes per formula unit (*V*/*Z*) and Na site occupancy ratios determined after different cycle numbers from the Rietveld refinement of *ex situ* XRPD patterns described in the *R*-3*c* space group.

Cycling condition	*a* (Å)	*c* (Å)	*c*/*a*	*V*/*Z* (Å^3)	Na(1) Occ.	Na(2) Occ.	Total Na /f.u.
Pristine	8.9652(3)	21.4824(10)	2.396	249.217(18)	0.95(4)	0.973(13)	3.87(7)
1st ch. at 4.3 V	8.3840(2)	21.8774(8)	2.609	221.692(10)	0.71(3)	0.20(2)	1.30(10)
5th ch. at 4.3 V	8.5463(3)	21.9482(14)	2.568	231.387(19)	0.47(6)	0.28(2)	1.31(13)
5th disch. at 2 V	8.9087(3)	21.7102(13)	2.437	248.70(2)	-	-	-

The aged electrodes recovered after the end of the fifth charge at 4.3 V and fifth discharge at 2.0 V were also examined by XAS. The Mn and V K-edges XANES and FTs for aged samples are compared with those of the pristine material and the material recovered after the first charge in **Figure 13**. Concerning the Mn K-edge XANES spectrum on the sample after the 5th discharge, it displays an edge position close to the Mn^{2+} reference although its shape is different compared to that of the pristine. After the 5th charge, however, Mn could not be fully oxidized to Mn^{3+}, but to an average oxidation state limited to around $Mn^{2.5+}$. Moreover, six regular Mn-O bonds of 2.115(5) Å are required to describe the Mn environment for the sample after the 5th discharge (**Table 6**), which is close to that in the pristine material with a Mn-O bond of 2.138(5) Å. Considering the FTs of the sample after the 5th charge, the intensity of the main peak shows a more decreased intensity: four equatorial Mn-O bonds of 1.911(5) Å and two elongated axial Mn-O bonds of 2.168(5) Å were necessary to describe the Mn environment, confirming the occurrence of Jahn-Teller distortion related to the presence of Mn^{3+}. It is important to recall that also in this case the presence of Jahn-Teller distortion is not inducing dramatic changes in the pre-peak region, which is in good agreement with the previous studies[52,54–56] of Mn^{3+} containing materials.

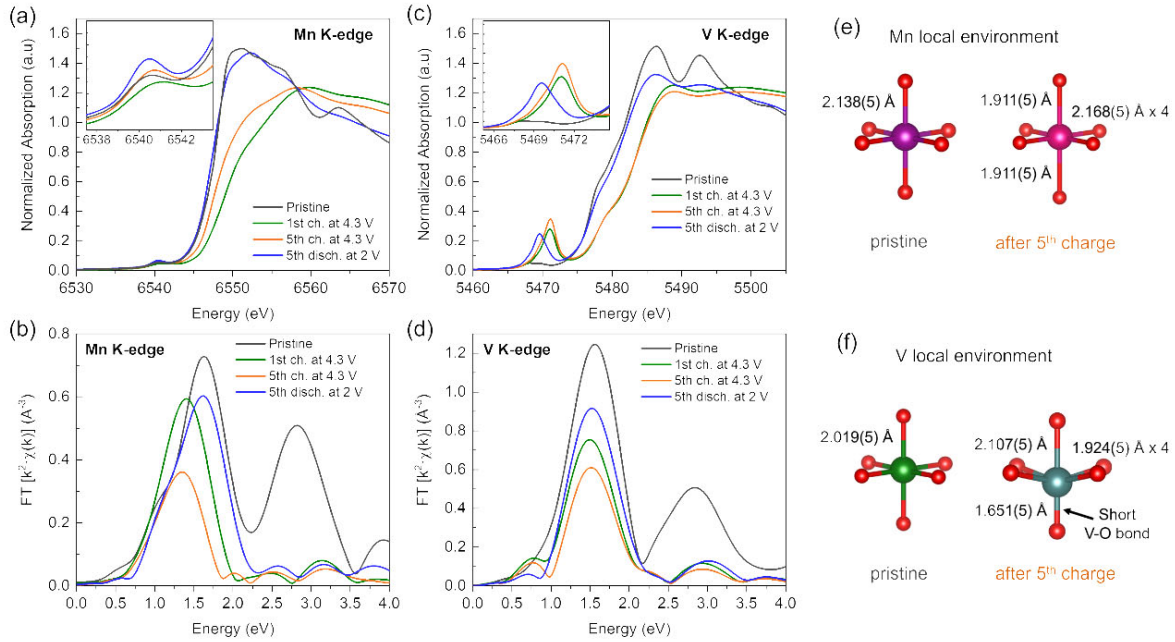

Figure 13. XAS of the pristine material $Na_4MnV(PO_4)_3$, and of the materials recovered after the first charge, the fifth charge and the fifth discharge, when cycled between 2 and 4.3 V vs. Na^+/Na. XANES spectra at the **(a)** Mn K-edge and **(b)** V K-edge. Fourier transforms of the EXAFS oscillations extracted at the **(c)** Mn K-edge and **(d)** V K-edge. (**e-f**) local environments of Mn and V in the pristine state and after the 5th charge.

Table 6. Refined Mn-O and V-O distances in the first coordination shells as determined by EXAFS analysis of the spectra collected for $Na_4MnV(PO_4)_3$ recovered after the fifth charge and the fifth discharge, when cycled between 2 and 4.3 V vs. Na^+/Na.

Cycling condition	N	σ^2 (Å^2)	R-factor	Mn-O (Å)	N	σ^2 (Å^2)	R-factor	V-O (Å)
5th ch. at 4.3 V	4	0.0117	0.0029	1.911(5)	4	0.0050	0.0060	1.924(5)
					1			1.651(5)
	2			2.168(5)	1			2.107(5)
5th disch. at 2 V	6	0.0129	0.0106	2.115(5)	5	0.0060	0.0021	2.010(5)
					1			1.647(5)

At the V K-edge, all the XANES spectra collected on the aged electrodes show much pronounced pre-edges when compared with those of the pristine material indicating that the V environment became much distorted. From the EXAFS analysis of the spectrum collected at the V K-edge, five regular V-O bonds of 2.010(5) Å and one short V-O bond of 1.647(5) Å were required to describe the V average environment

after the fifth discharge. Thus, the not fully reduced vanadium can be associated to the short V-O bond. For comparison, the [5.5+0.5] coordination model was suitable to describe the average local environment of V after one cycle. As the electrode material is being aged, the number of distorted environments increases for V. The EXAFS analysis for the sample recovered after the 5th charge indicates that a distorted VO_6 octahedral environment is well described using a [4+1+1] coordination model, with four equatorial bonds of 1.924(5) Å, one short bond of 1.651(5) Å, and one long bond of 2.107(5) Å.

The ageing mechanism of V-based NASICON materials related to the migration of transition metals was addressed by several research groups,[29,34,57] especially, when the $V^{5+/4+}$ redox couple is activated. Liu *et al*.[34] suggested possible migration of vanadium ions to the partially emptied Na(1) site, when a $Na_3CrV(PO_4)_3$ electrode is cycled between 2.5 and 4.3 V thus involving the activation of the $V^{5+/4+}$ redox couple. This could be either suppressed or partially restored when it is cycled at low temperature (-15 °C) or over-discharged to low voltage (1.4 V vs. Na^+/Na) as evidenced by HAADF-STEM.[34] Similarly, the anti-site mixing between V^{5+} and Li^+ ions in a $Li_3V_2(PO_4)_3$ electrode above 4.5 V vs. Li^+/Li was suggested by Kim *et al*.,[57] although the structure of $Li_3V_2(PO_4)_3$ is anti-NASICON. In contrast, the results of DFT-based calculations by Wang *et al*.[29] suggested that the migration of the transition metals (Cr or V) in $Na_1MnCr(PO_4)_3$ and $Na_1MnV(PO_4)_3$ NASICON materials was unlikely to occur due to the high energy penalty of transition metal migration. Further investigations are required to better understand the migration of the transition metals in NASICON-type materials.

Continuing to address the aging mechanism, it was suggested that amorphization in $Na_4MnV(PO_4)_3$ occurred upon cycling with extended voltage windows, as the redox reaction becomes more difficult when the charge transfer resistance increases and the diffusion coefficient decreases.[23] However, when it comes to the local environment aspect, the structural modifications from the symmetric Mn and V environments to Mn^{3+} Jahn-Teller and vanadyl-type distortions can also play critical contributions to the ageing mechanism. Lowering the cut-off voltage to 1 V can lead to partial structural recovery after the first cycle, but this could not prevent the structural degradation in

the following cycles probably due to depopulated Na(1) site (leading to dramatic increase in the *c* parameter) and highly distorted Mn and V local environments. In addition, battery operation at low voltage can increase dramatically impedance.[58]

Conclusion

To sum up, the Na^+ extraction/insertion mechanism of $Na_4MnV(PO_4)_3$ including the structural changes at local and long range scales were discussed. Both local and long range structures are highly reversible when a battery cell is cycled limiting the exchange of two Na^+ ions within the voltage window of 2-3.75 V vs. Na^+/Na. When the third Na^+ is extracted by extending the upper cut-off voltage to 4.3 V, irreversible structural modifications occur, which are partially restored when the lower cut-off voltage is decreased down to 1 V. Na^+ extraction within the extended voltage window up to 4.3 V occurs according to three potential domains successively through a solid solution reaction, a two phase reaction and a solid solution reaction with the activation of the $V^{4+/3+}$, $Mn^{3+/2+}$, and $V^{5+/4+}$ redox couples, respectively. When more than half of V^{3+} ions are oxidized to V^{4+}, symmetry lowering is observed from the *R*-3*c* to the *R*32 space group resulting in two environments for the transition metal ions, with M-O distances of 2.127(15) and 2.032(15) Å in $Na_3MnV(PO_4)_3$ composition.

When the $V^{5+/4+}$ redox couple is activated during charge, remarkable structural modifications occur at local and long range scales: Depopulation of the Na(1) site, dramatic increase in the *c* parameter, Jahn-Teller distortion of the Mn local environment and vanadyl-like short bonds in V local environment. As a result of this, the electrochemical reaction mechanism changes to a complete solid solution during discharge with a simultaneous reduction of Mn and V to Mn^{2+} and V^{3+}, respectively. As the structure degradations proceed, the redox reactions of manganese and vanadium are not fully activated compared to those before the ageing of the material. Mn is only oxidized to $Mn^{2.5+}$ after the fifth charge, and V cannot be completely reduced to V^{3+} but $V^{3.2+}$ after the fifth discharge when cycled between 2 and 4.3 V, together with further distortion of MnO_6 and VO_6 octahedral environments.

Supporting Information

SEM images, SXRPD patterns, TGA measurement, Adiabatic calorimetry, Refined structural parameters, electrochemical cycling performance, *operando* SXRPD measurement

Acknowledgements

The authors thank Fan Chen (LRCS) and Jacob Olchowka (ICMCB) for fruitful discussion, as well as Cathy Denage and Emmanuel Petit (ICMCB) for technical support. The authors acknowledge ALBA (Barcelona, Spain) for synchrotron X-ray diffraction experiments on the MSPD beamline (proposal number 20200024218). XAS experiments were performed on the ROCK beamline (financed by the French National Research Agency (ANR) as a part of the “Investissements d’Avenir” program, reference: ANR-10-EQPX-45) at SOLEIL Synchrotron, France. They are also grateful to the ANRT and TIAMAT for the funding (CIFRE grant) of S. P.'s PhD thesis, and acknowledge the financial support of Région Nouvelle Aquitaine and of the French National Research Agency (STORE-EX Labex Project ANR-10-LABX-76-01).

References

(1) Liu, R.; Liang, Z.; Gong, Z.; Yang, Y. Research Progress in Multielectron Reactions in Polyanionic Materials for Sodium-Ion Batteries. *Small Methods* **2019**, *3* (4), 1800221. https://doi.org/10.1002/smtd.201800221.

(2) Chen, S.; Wu, C.; Shen, L.; Zhu, C.; Huang, Y.; Xi, K.; Maier, J.; Yu, Y. Challenges and Perspectives for NASICON-Type Electrode Materials for Advanced Sodium-Ion Batteries. *Adv. Mater.* **2017**, *29* (48), 1–21. https://doi.org/10.1002/adma.201700431.

(3) Avdeev, M. Crystal Chemistry of NaSICONs: Ideal Framework, Distortion, and Connection to Properties. *Chem. Mater.* **2021**, *33* (19), 7620–7632. https://doi.org/10.1021/acs.chemmater.1c02695.

(4) Singh, B.; Wang, Z.; Park, S.; Gautam, G. S.; Chotard, J. N.; Croguennec, L.; Carlier, D.; Cheetham, A. K.; Masquelier, C.; Canepa, P. A Chemical Map of NaSICON Electrode Materials for Sodium-Ion Batteries. *J. Mater. Chem. A* **2021**, *9* (1), 281–292. https://doi.org/10.1039/d0ta10688g.

(5) Masquelier, C.; Croguennec, L. Polyanionic (Phosphates, Silicates, Sulfates) Frameworks as Electrode Materials for Rechargeable Li (or Na) Batteries. *Chem. Rev.* **2013**, *113* (8), 6552–6591. https://doi.org/10.1021/cr3001862.

(6) Hasa, I.; Mariyappan, S.; Saurel, D.; Adelhelm, P.; Koposov, A. Y.; Masquelier, C.; Croguennec, L.; Casas-Cabanas, M. Challenges of Today for Na-Based Batteries of the Future: From Materials to Cell Metrics. *J. Power Sources* **2021**, *482* (August 2020), 228872. https://doi.org/10.1016/j.jpowsour.2020.228872.

(7) Lyu, Y.; Liu, Y.; Yu, Z. E.; Su, N.; Liu, Y.; Li, W.; Li, Q.; Guo, B.; Liu, B. Recent Advances in High Energy-Density Cathode Materials for Sodium-Ion Batteries. *Sustain. Mater. Technol.* **2019**, *21*, 1–21. https://doi.org/10.1016/j.susmat.2019.e00098.

(8) UEBOU, Y.; KIYABU, T.; OKADA, S.; YAMAKI, J.; 上坊泰史; 木藪敏康; 岡田重人; 山木準一; ウエボウヤスシ; キヤブトシヤス; オカダシゲト; ヤマキジュンイチ. Electrochemical Sodium Insertion into the 3D-Framework of Na_3M_2(PO_4)_3 (M=Fe, V). *reports Inst. Adv. Mater. Study Kyushu Univ.*

2002, *16*, 1–5.

(9) Saravanan, K.; Mason, C. W.; Rudola, A.; Wong, K. H.; Balaya, P. The First Report on Excellent Cycling Stability and Superior Rate Capability of Na3V2(PO4)3 for Sodium Ion Batteries. *Adv. Energy Mater.* **2013**, *3* (4), 444–450. https://doi.org/10.1002/aenm.201200803.

(10) Wang, Z.; Park, S.; Deng, Z.; Carlier, D.; Chotard, J. N.; Croguennec, L.; Gautam, G. S.; Cheetham, A. K.; Masquelier, C.; Canepa, P. Phase Stability and Sodium-Vacancy Orderings in a NaSICON Electrode. *J. Mater. Chem. A* **2022**, *10* (1), 209–217. https://doi.org/10.1039/d1ta09249a.

(11) Lim, S. Y.; Kim, H.; Shakoor, R. A.; Jung, Y.; Choi, J. W. Electrochemical and Thermal Properties of NASICON Structured Na 3 V 2 (PO 4) 3 as a Sodium Rechargeable Battery Cathode: A Combined Experimental and Theoretical Study . *J. Electrochem. Soc.* **2012**, *159* (9), A1393–A1397. https://doi.org/10.1149/2.015209jes.

(12) Park, S.; Wang, Z.; Deng, Z.; Moog, I.; Canepa, P.; Fauth, F.; Carlier, D.; Croguennec, L.; Masquelier, C.; Chotard, J. N. Crystal Structure of Na2V2(PO4)3, an Intriguing Phase Spotted in the Na3V2(PO4)3-Na1V2(PO4)3System. *Chem. Mater.* **2022**, *34* (1), 451–462. https://doi.org/10.1021/acs.chemmater.1c04033.

(13) Park, S.; Chotard, J. N.; Carlier, D.; Moog, I.; Courty, M.; Duttine, M.; Fauth, F.; Iadecola, A.; Croguennec, L.; Masquelier, C. Crystal Structures and Local Environments of NASICON-Type Na3FeV(PO4)3and Na4FeV(PO4)3positive Electrode Materials for Na-Ion Batteries. *Chem. Mater.* **2021**, *33* (13), 5355–5367. https://doi.org/10.1021/acs.chemmater.1c01457.

(14) Hadouchi, M.; Yaqoob, N.; Kaghazchi, P.; Tang, M.; Liu, J.; Sang, P.; Fu, Y.; Huang, Y.; Ma, J. Fast Sodium Intercalation in Na3.41£0.59FeV(PO4)3: A Novel Sodium-Deficient NASICON Cathode for Sodium-Ion Batteries. *Energy Storage Mater.* **2021**, *35* (November 2020), 192–202. https://doi.org/10.1016/j.ensm.2020.11.010.

(15) de Boisse, B. M.; Ming, J.; Nishimura, S.; Yamada, A. Alkaline Excess Strategy to NASICON-Type Compounds towards Higher-Capacity Battery Electrodes. *J. Electrochem. Soc.* **2016**, *163* (7), A1469–A1473. https://doi.org/10.1149/2.0041608jes.

(16) Xu, C.; Zhao, J.; Wang, E.; Liu, X. X.; Shen, X.; Rong, X.; Zheng, Q.; Ren, G.; Zhang, N.; Liu, X. X.; Guo, X.; Yang, C.; Liu, H.; Zhong, B.; Hu, Y. S. A Novel NASICON-Typed Na4VMn0.5Fe0.5(PO4)3 Cathode for High-Performance Na-Ion Batteries. *Adv. Energy Mater.* **2021**, *11* (22), 1–9. https://doi.org/10.1002/aenm.202100729.

(17) Zhou, W.; Xue, L.; Lü, X.; Gao, H.; Li, Y.; Xin, S.; Fu, G.; Cui, Z.; Zhu, Y.; Goodenough, J. B. NaxMV(PO4)3 (M = Mn, Fe, Ni) Structure and Properties for Sodium Extraction. *Nano Lett.* **2016**, *16* (12), 7836–7841. https://doi.org/10.1021/acs.nanolett.6b04044.

(18) Chen, F.; Kovrugin, V. M.; David, R.; Mentré, O.; Fauth, F.; Chotard, J.-N.; Masquelier, C. A NASICON-Type Positive Electrode for Na Batteries with High Energy Density: Na $_4$ MnV(PO $_4$) $_3$. *Small Methods* **2018**, *1800218*, 1800218. https://doi.org/10.1002/smtd.201800218.

(19) Zakharkin, M. V; Drozhzhin, O. A.; Tereshchenko, I. V; Chernyshov, D.; Abakumov, A. M.; Antipov, E. V; Stevenson, K. J. Enhancing Na+ Extraction Limit through High Voltage Activation of the NASICON-Type Na4MnV(PO4)3 Cathode. *ACS Appl. Energy Mater.* **2018**, *1*, 5842–5846. https://doi.org/10.1021/acsaem.8b01269.

(20) Zakharkin, M. V.; Drozhzhin, O. A.; Ryazantsev, S. V.; Chernyshov, D.; Kirsanova, M. A.; Mikheev, I. V.; Pazhetnov, E. M.; Antipov, E. V.; Stevenson, K. J.; Antipov, V.; Stevenson, K. J. Electrochemical Properties and Evolution of the Phase Transformation Behavior in the NASICON-Type Na3+xMnxV2-x(PO4)3 (0≤x≤1) Cathodes for Na-Ion Batteries. *J. Power Sources* **2020**, *470* (February), 228231. https://doi.org/10.1016/j.jpowsour.2020.228231.

(21) Xu, C.; Xiao, R.; Zhao, J.; Ding, F.; Yang, Y.; Rong, X.; Guo, X.; Yang, C.; Liu, H.; Zhong, B.; Hu, Y. S. Mn-Rich Phosphate Cathodes for Na-Ion Batteries with Superior Rate Performance. *ACS Energy Lett.* **2022**, *7* (1), 97–107. https://doi.org/10.1021/acsenergylett.1c02107.

(22) Soundharrajan, V.; Nithiananth, S.; Sakthiabirami, K.; Kim, J. H.; Su, C. Y.; Chang, J. K. The Advent of Manganese-Substituted Sodium Vanadium Phosphate-Based Cathodes for Sodium-Ion Batteries and Their Current Progress: A Focused Review. *J. Mater. Chem. A* **2022**, *10* (3), 1022–1046. https://doi.org/10.1039/d1ta09040b.

(23) Buryak, N. S.; Anishchenko, D. V; Levin, E. E.; Ryazantsev, S. V; Martin-diaconescu, V.; Zakharkin, M. V; Nikitina, V. A.; Antipov, E. V. High-Voltage Structural Evolution and Its Kinetic Consequences for the Na 4 MnV (PO 4) 3 Sodium-Ion Battery Cathode Material. *J. Power Sources* **2022**, *518* (August 2021), 230769. https://doi.org/10.1016/j.jpowsour.2021.230769.

(24) Anishchenko, D. V.; Zakharkin, M. V.; Nikitina, V. A.; Stevenson, K. J.; Antipov, E. V. Phase Boundary Propagation Kinetics Predominately Limit the Rate Capability of NASICON-Type Na3+xMnxV2-x(PO4)3 (0≤x≤1) Materials. *Electrochim. Acta* **2020**, *354, 136761-136766*. https://doi.org/10.1016/j.electacta.2020.136761.

(25) Ghosh, S.; Barman, N.; Mazumder, M.; Pati, S. K.; Rousse, G.; Senguttuvan, P. High Capacity and High-Rate NASICON-Na3.75V1.25Mn0.75(PO4)3 Cathode for Na-Ion Batteries via Modulating Electronic and Crystal Structures. *Adv. Energy Mater.* **2020**, *10* (6), 1–11. https://doi.org/10.1002/aenm.201902918.

(26) Zhang, J.; Liu, Y.; Zhao, X.; He, L.; Liu, H.; Song, Y.; Sun, S.; Li, Q.; Xing, X.; Chen, J. A Novel NASICON-Type Na4MnCr(PO4)3 Demonstrating the Energy Density Record of Phosphate Cathodes for Sodium-Ion Batteries. *Adv. Mater.* **2020**, *32* (11), 1–8. https://doi.org/10.1002/adma.201906348.

(27) Zhao, Y.; Gao, X.; Gao, H.; Dolocan, A.; Goodenough, J. B. Elevating Energy Density for Sodium-Ion Batteries through Multielectron Reactions. *Nano Lett.* **2021**. 21 (5), 2281–2287. https://doi.org/10.1021/acs.nanolett.1c00100.

(28) Zhang, W.; Li, H.; Zhang, Z.; Xu, M.; Lai, Y.; Chou, S. L. Full Activation of Mn4+/Mn3+ Redox in Na4MnCr(PO4)3 as a High-Voltage and High-Rate Cathode Material for Sodium-Ion Batteries. *Small* **2020**, *16* (25), 1–8. https://doi.org/10.1002/smll.202001524.

(29) Wang, J.; Wang, Y.; Seo, D. H.; Shi, T.; Chen, S.; Tian, Y.; Kim, H.; Ceder, G. A High-Energy NASICON-Type Cathode Material for Na-Ion Batteries. *Adv. Energy Mater.* **2020**, *1903968*, 1–10. https://doi.org/10.1002/aenm.201903968.

(30) Zhang, J.; Zhao, X.; Song, Y.; Li, Q.; Liu, Y.; Chen, J.; Xing, X. Understanding the Superior Sodium-Ion Storage in a Novel Na3.5Mn0.5V1.5(PO4)3 Cathode. *Energy Storage Mater.* **2019**, *23* (May), 25–34. https://doi.org/10.1016/j.ensm.2019.05.041.

(31) Ghosh, S.; Barman, N.; Senguttuvan, P. Impact of Mg2+ and Al3+ Substitutions

on the Structural and Electrochemical Properties of NASICON-NaxVMn0.75M0.25(PO4)3 (M = Mg and Al) Cathodes for Sodium-Ion Batteries. *Small* **2020**, *3*, 1–8. https://doi.org/10.1002/smll.202003973.

(32) Lavela, P.; Klee, R.; Hidalgo, M. A.; Tirado, J. L. Iron Substitution in Na4VMn(PO4)3 as a Strategy for Improving the Electrochemical Performance of Sodium-Ion Batteries. *J. Electroanal. Chem.* **2021**, *895* (May), 115533. https://doi.org/10.1016/j.jelechem.2021.115533.

(33) Wu, B.; Hou, G.; Kovalska, E.; Mazanek, V.; Marvan, P.; Liao, L.; Dekanovsky, L.; Sedmidubsky, D.; Marek, I.; Hervoches, C.; Sofer, Z. High-Entropy NASICON Phosphates (Na3M2(PO4)3and NaMPO4Ox, M = Ti, V, Mn, Cr, and Zr) for Sodium Electrochemistry. *Inorg. Chem.* **2022**, *61* (9), 4092–4101. https://doi.org/10.1021/acs.inorgchem.1c03861.

(34) Liu, R.; Zheng, S.; Yuan, Y.; Yu, P.; Liang, Z.; Zhao, W.; Shahbazian-Yassar, R.; Ding, J.; Lu, J.; Yang, Y. Counter-Intuitive Structural Instability Aroused by Transition Metal Migration in Polyanionic Sodium Ion Host. *Adv. Energy Mater.* **2021**, *11* (3), 1–9. https://doi.org/10.1002/aenm.202003256.

(35) Fauth, F.; Peral, I.; Popescu, C.; Knapp, M. The New Material Science Powder Diffraction Beamline at ALBA Synchrotron. *Powder Diffr.* **2013**, *28* (September), S360–S370.

(36) Herklotz, M.; Weiß, J.; Ahrens, E.; Yavuz, M.; Mereacre, L.; Kiziltas-Yavuz, N.; Dräger, C.; Ehrenberg, H.; Eckert, J.; Fauth, F.; Giebeler, L.; Knapp, M. A Novel High-Throughput Setup for in Situ Powder Diffraction on Coin Cell Batteries. *J. Appl. Crystallogr.* **2016**, *49*, 340–345. https://doi.org/10.1107/S1600576715022165.

(37) Rodríguez-Carvajal, J. Recent Advances in Magnetic Structure Determination by Neutron Powder Diffraction. *Phys. B Phys. Condens. Matter* **1993**, *192* (1–2), 55–69. https://doi.org/10.1016/0921-4526(93)90108-I.

(38) Briois, V.; La Fontaine, C.; Belin, S.; Barthe, L.; Moreno, T.; Pinty, V.; Carcy, A.; Girardot, R.; Fonda, E. ROCK: The New Quick-EXAFS Beamline at SOLEIL. *J. Phys. Conf. Ser.* **2016**, *712* (1). https://doi.org/10.1088/1742-6596/712/1/012149.

(39) Leriche, J. B.; Hamelet, S.; Shu, J.; Morcrette, M.; Masquelier, C.; Ouvrard, G.; Zerrouki, M.; Soudan, P.; Belin, S.; Elkaïm, E.; Baudelet, F. An Electrochemical

Cell for Operando Study of Lithium Batteries Using Synchrotron Radiation. *J. Electrochem. Soc.* **2010**, *157* (5), A606. https://doi.org/10.1149/1.3355977.

(40) Ravel, B.; Newville, M. ATHENA, ARTEMIS, HEPHAESTUS: Data Analysis for X-Ray Absorption Spectroscopy Using IFEFFIT. *J. Synchrotron Radiat.* **2005**, *12* (4), 537–541. https://doi.org/10.1107/S0909049505012719.

(41) Fang, J.; Wang, S.; Yao, X.; Hu, X.; Wang, Y.; Wang, H. Ration Design of Porous Mn-Doped Na3V2(PO4)3 Cathode for High Rate and Super Stable Sodium-Ion Batteries. *Electrochim. Acta* **2019**, *295*, 262–269. https://doi.org/10.1016/j.electacta.2018.10.150.

(42) Li, H.; Jin, T.; Chen, X.; Lai, Y.; Zhang, Z.; Bao, W.; Jiao, L. Rational Architecture Design Enables Superior Na Storage in Greener NASICON-Na4MnV(PO4)3 Cathode. *Adv. Energy Mater.* **2018**, *8* (24), 1–9. https://doi.org/10.1002/aenm.201801418.

(43) Gao, X.; Lian, R.; He, L.; Fu, Q.; Indris, S.; Schwarz, B.; Wang, X.; Chen, G.; Ehrenberg, H.; Wei, Y. Phase Transformation, Charge Transfer, and Ionic Diffusion of Na4MnV(PO4)3in Sodium-Ion Batteries: A Combined First-Principles and Experimental Study. *J. Mater. Chem. A* **2020**, *8* (34), 17477–17486. https://doi.org/10.1039/d0ta05929c.

(44) Nisar, U.; Shakoor, R. A.; Essehli, R.; Amin, R.; Orayech, B.; Ahmad, Z.; Kumar, P. R.; Kahraman, R.; Al-Qaradawi, S.; Soliman, A. Sodium Intercalation/de-Intercalation Mechanism in Na 4 MnV(PO 4) 3 Cathode Materials. *Electrochim. Acta* **2018**, *292*, 98–106. https://doi.org/10.1016/j.electacta.2018.09.111.

(45) Perfilyeva, T. I.; Drozhzhin, O. A.; Alekseeva, A. M.; Zakharkin, M. V.; Mironov, A. V.; Mikheev, I. V.; Bobyleva, Z. V.; Marenko, A. P.; Marikutsa, A. V.; Abakumov, A. M.; Antipov, E. V. Complete Three-Electron Vanadium Redox in NASICON-Type Na3VSc(PO4)3 Electrode Material for Na-Ion Batteries. *J. Electrochem. Soc.* **2021**, *168* (11), 110550. https://doi.org/10.1149/1945-7111/ac393d.

(46) Senguttuvan, P.; Rousse, G.; Dompablo, M. E. A. De; Vezin, H.; Tarascon, J.; Palacín, M. R. Supplementary Information: Low Potential Sodium Insertion in NASICON-Type Structure through the Ti (III)/ Ti (II) Redox Couple. *J. Am. Chem. Soc.* **2013**, No. Iii, 1–6.

(47) Masquelier, C.; Wurm, C.; Rodríguez-Carvajal, J.; Gaubicher, J.; Nazar, L. A

Powder Neutron Diffraction Investigation of the Two Rhombohedral NASICON Analogues: γ-Na3Fe2(PO4)3 and Li3Fe2(PO4)3. *Chem. Mater.* **2000**, *12* (2), 525–532. https://doi.org/10.1021/cm991138n.

(48) Gaubicher, J.; Wurm, C.; Goward, G.; Masquelier, C.; Nazar, L. Rhombohedral Form of Li3V2(PO4)3 as a Cathode in Li-Ion Batteries. *Chem. Mater.* **2000**, *12* (11), 3240–3242. https://doi.org/10.1021/cm000345g.

(49) Park, S.; Chotard, J.-N.; Carlier, D.; Moog, I.; Duttine, M.; Ois Fauth, F.; Iadecola, A.; Croguennec, L.; Masquelier, C. An Asymmetric Sodium Extraction/Insertion Mechanism for the Fe/V-Mixed NASICON Na4FeV(PO4)3. *Chem. Mater.* **2022**, *34* (9), 4142–4152. https://doi.org/10.1021/ACS.CHEMMATER.2C00501.

(50) Liu, R.; Xu, G.; Li, Q.; Zheng, S.; Zheng, G.; Gong, Z.; Li, Y.; Kruskop, E.; Fu, R.; Chen, Z.; Amine, K.; Yang, Y. Exploring Highly Reversible 1.5-Electron Reactions (V 3+ /V 4+ /V 5+) in Na 3 VCr(PO 4) 3 Cathode for Sodium-Ion Batteries . *ACS Appl. Mater. Interfaces* **2017**, *9* (50), 43632–43639. https://doi.org/10.1021/acsami.7b13018.

(51) Zatovsky, I. V.; Strutynska, N. Y.; Ogorodnyk, I. V.; Baumer, V. N.; Slobodyanik, N. S.; Yatskin, M. M.; Odynets, I. V. Peculiarity of Formation of the NASICON-Related Phosphates in the Space Group R32: Synthesis and Crystal Structures of Na4MIIAl(PO4)3 (MII-Mg, Mn). *Struct. Chem.* **2016**, *27* (1), 323–330. https://doi.org/10.1007/s11224-015-0713-6.

(52) Aquilanti, G.; Giorgetti, M.; Dominko, R.; Mino, L.; Agostini, G.; Borfecchia, E.; Iadecola, A.; Perea, A.; Aldon, L.; Aquilanti, G. Li Deinsertion Mechanism and Jahn – Teller x-Ray Absorption Spectroscopy Investigation. *J. Phys. D. Appl. Phys.* **2017**, **50** 144004- 144013.

(53) Bai, X.; Sathiya, M.; Mendoza-Sánchez, B.; Iadecola, A.; Vergnet, J.; Dedryvère, R.; Saubanère, M.; Abakumov, A. M.; Rozier, P.; Tarascon, J. M. Anionic Redox Activity in a Newly Zn-Doped Sodium Layered Oxide P2-Na2/3Mn1−yZnyO2 (0 < y < 0.23). *Adv. Energy Mater.* **2018**, *8* (32), 1–12. https://doi.org/10.1002/aenm.201802379.

(54) García, J.; Subías, G.; Sánchez, M. C.; Blasco, J. Jahn-Teller Dynamic Distortions in LaMnO3 Determined by EXAFS. *Phys. Scr. T* **2005**, *T115*, 594–596. https://doi.org/10.1238/Physica.Topical.115a00594.

(55) Piper, L. F. J.; Quackenbush, N. F.; Sallis, S.; Scanlon, D. O.; Watson, G. W.; Nam, K.-W.; Yang, X.-Q.; Smith, K. E.; Omenya, F.; Chernova, N. A.; Whittingham, M. S. Elucidating the Nature of Pseudo Jahn − Teller Distortions in Li. *J. Phys. Chem. C* **2013**, *117*, 10383–10396.

(56) Cuartero, V.; Blasco, J.; Subías, G.; García, J.; Meneghini, C.; Aquilanti, G. Stability of Jahn-Teller Distortion Ordering in LaM N1-x S Cx O3. *Phys. Rev. B - Condens. Matter Mater. Phys.* **2015**, *92* (12), 1–10. https://doi.org/10.1103/PhysRevB.92.125118.

(57) Kim, S.; Zhang, Z.; Wang, S.; Yang, L.; Cairns, E. J.; Penner-Hahn, J. E.; Deb, A. Electrochemical and Structural Investigation of the Mechanism of Irreversibility in Li3V2(PO4)3 Cathodes. *J. Phys. Chem. C* **2016**, *120* (13), 7005–7012. https://doi.org/10.1021/acs.jpcc.6b00408.

(58) Zhao, Y.; Gao, X.; Gao, H.; Jin, H.; Goodenough, J. B. Three Electron Reversible Redox Reaction in Sodium Vanadium Chromium Phosphate as a High-Energy-Density Cathode for Sodium-Ion Batteries. *Adv. Funct. Mater.* **2020**, *2*, 3–9. https://doi.org/10.1002/adfm.201908680.

TOC GRAPHIC

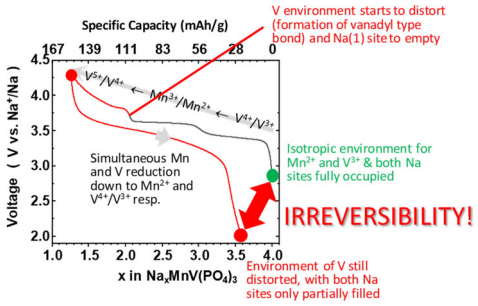
Specific Capacity (mAh/g)
167 139 111 83 56 28 0
Voltage (V vs. Na+/Na)
4.5 4.0 3.5 3.0 2.5 2.0
V5+/V4+
Mn3+/Mn2+
V4+/V3+
Simultaneous Mn and V reduction down to Mn2+ and V4+/V3+ resp.
1.0 1.5 2.0 2.5 3.0 3.5 4.0
x in NaxMnV(PO4)3
V environment starts to distort (formation of vanadyl type bond) and Na(1) site to empty
Isotropic environment for Mn2+ and V3+ & both Na sites fully occupied
IRREVERSIBILITY!
Environment of V still distorted, with both Na sites only partially filled